REVIEWS

Micromachined High-Resolution Accelerometers

Girish Krishnan[1], Chaitanya U. Kshirsagar[2], G. K. Ananthasuresh[1] AND Navakanta Bhat[2]

Abstract | In this paper, we review the high-resolution, micromachined accelerometers by enunciating the development of their mechanical components, the electronic circuitry and the microfabrication processes. A survey of the literature suggests that the research in this area is mostly focused on improving microfabrication and electronic circuitry. The resolution of the accelerometers is dependent on the sensitivity of the mechanical components as well as the ability of the electronic circuitry in suppressing the noise. The noise comes from mechanical components as well as electronic circuitry and plays a detrimental role in achieving high resolution. This is reviewed in this paper after explaining the working principles of selected high-resolution micromachined accelerometers. Sensing acceleration by measuring the change in capacitance is widely used but it has many complications. These are discussed in detail by presenting various techniques for sensing capacitance. The microfabrication processes that dictate the design are reviewed by tracking the evolution of high-resolution accelerometers found in the literature and comparing their sensitivities and resolutions. This paper gives an account of the significant accomplishments, some challenges for the future, and a few novel concepts in achieving high resolution of the order of a millionth of *g*, the acceleration due to gravity.

1. Introduction

The emergence of silicon microfabrication techniques has enabled miniaturization and batch fabrication of a number of sensors. This has resulted in an increase in their market viability and reduction in costs in addition to enhanced performance in most cases[1]. Accelerometers are some of the first sensors, whose miniaturization and subsequent cost-reduction have paved the way for their use in a number of applications[2,3]. From being used as sensors to deploy air bags in automobiles to inertial navigation and other consumer applications, micromachined accelerometers of varying specifications are found in different applications today. They all differ, as required by the specifications of their applications, in their resolution, range, and bandwidth as well as the principle of transduction and microfabrication.

Typical ranges of acceleration for different applications are shown in Fig. 1 against the required bandwidth. High resolution may be needed in all of these applications depending on a specific task at hand. For example, as high a resolution as *micro-g* (i.e., one millionth of the acceleration due to gravity, i.e., $10^{-6} \times 9.81$ m/s^2) is needed not only in space and inertial navigation applications but also in vibration monitoring to detect human footsteps for surveillance applications and for precise guidance in ballistics. Accelerometers of low to medium resolution have been reviewed in

[1]*Mechanical Engineering, Indian Institute of Science, Bangalore, India*
[2]*Electrical Communication Engineering, Indian Institute of Science, Bangalore, India*
suresh@mecheng.iisc.ernet.in

Figure 1: Range vs. bandwidths required for various applications. (An enhanced version of the data given in S. Reyntjens PhD thesis at Katholieke Universiteit Leuven, 2002.)
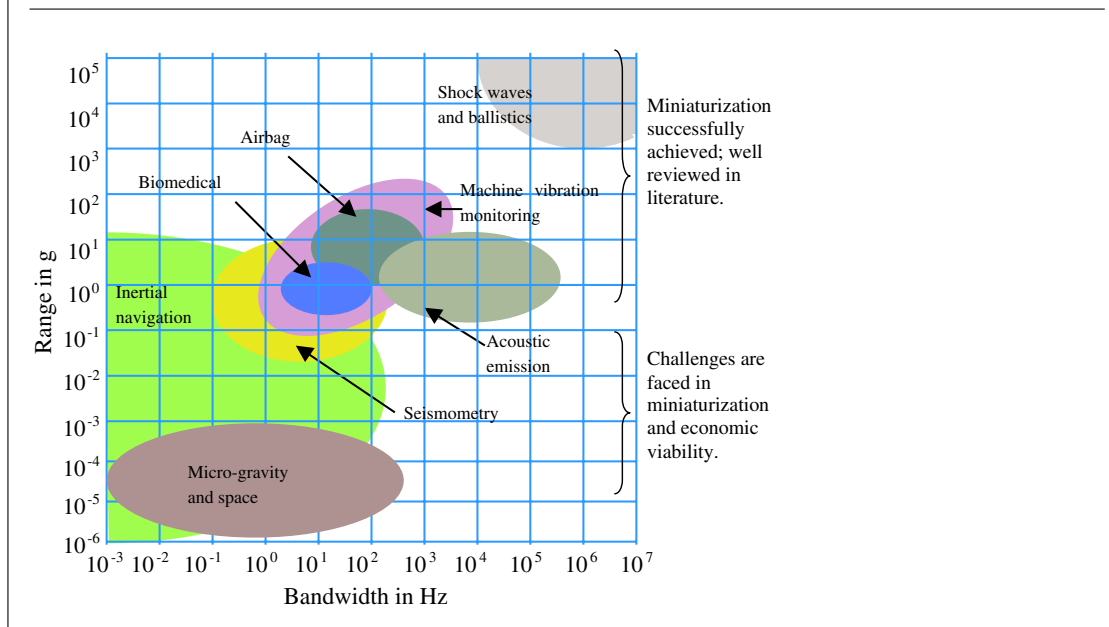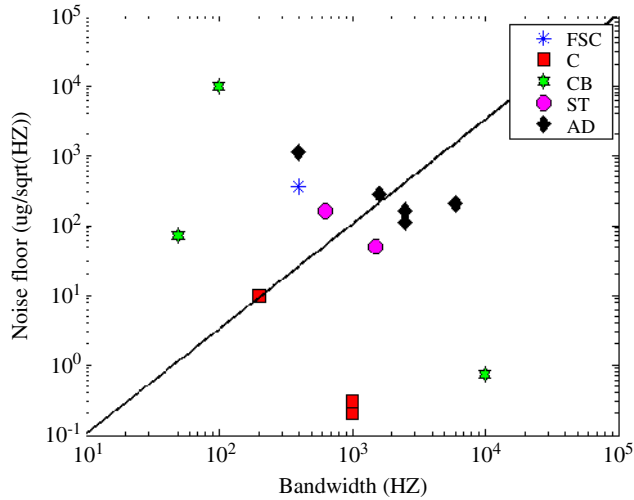
the literature[4,5]. Such accelerometers have been successfully miniaturized for applications such as air-bag sensors in automobiles, seismometry, vibration monitoring in machines, etc. On the other hand, miniaturization of high-resolution accelerometers has not been easy. There have been relatively few micro-*g* accelerometers reported in the literature[6—19]. There are many trade-offs in designing high-resolution accelerometers. Once successfully miniaturized and commercialized, these accelerometers might find widespread application in inertial navigation, in detecting micro-gravity in space, in achieving enhanced tilt-stabilization, and in consumer products such as camcorders, laptops, toys, etc. This paper gives an account of the relevant issues towards obtaining high resolution in accelerometers and attempts to present the evolution of microfarbication to the present state-of-the-art in fabricating them.

The basic working principle of most micromachined accelerometers is the same. They consist of a proof-mass attached to a compliant suspension. When an acceleration is applied, the proof-mass experiences an inertial force (D′ Alembert's force), which is equal to the mass times the value of the applied acceleration. This force causes the proof-mass to move and thereby elastically deforming the suspension. The amount of deflection is decided by the stiffness of the suspension. This deflection can be converted to a proportional change in the voltage by a number of transduction principles such as piezo-resistive[20,21],

capacitive[22], piezo-electric[23], electromagnetic[24], tunneling[15,16,25—29], optical[11,12,30], resonant[31,32], thermal[33], and others. Each of these types of sensing techniques needs electronic signal conditioning to convert the signal to an amplified analog or digital output. An overview of the different transduction principles, their applications, advantages, and shortcomings is given in Table 1. Many commercially available micromachined accelerometers use capacitive or piezoresistive principle. A few representative ones are shown in Figs. 2 and 3 in which the resolution is plotted against bandwidth and sensitivity, respectively. Note that the resolution is indicated as $g/\sqrt{Hz}$. This is because noise, which is an important factor that determines resolution, varies with the frequency of the acceleration signal in this manner. This will be discussed later in the paper. As can be seen in Fig. 3, high sensitivity does not automatically imply high resolution. The high-resolution accelerometers seen in Figs. 2 and 3 are currently very expensive.

High-resolution accelerometers need to be highly sensitive so that the signal produced due to the slightest change in the acceleration can be detected[34]. Sensitivity of the accelerometer is dependent on both the mechanical and the electronic sensitivities. Increasing the mechanical sensitivity by increasing the proof-mass size and reducing the suspension stiffness leads to low dynamic performance (bandwidth) and working range. The sensitivity of the electronic circuit depends upon the amplifier used and the techniques

Figure 2: Resolution Vs. bandwidth of some commercial micromachined accelerometers. FSC = Freescale semiconductors, C = Colybris, CB = Crossbow, ST = ST Microelectronics, and AD = Analog devices. The data shown is based on the specifications published by the respective companies at the time of this publication.

explained in detail in Section 2. That section also gives a brief description of other principles suitable for high-resolution sensing.

The noise aspects that limit the mechanical and electronic resolution of the accelerometer[13] are detailed in Section 3. It is found that the electronic noise is more dominant than the mechanical noise in the accelerometer system. Hence, it is sensible to make the mechanical components more sensitive in addition to efforts in improving the electronic noise floor. Sensitive mechanical components, with their huge proof-mass and long, thin, and narrow (and hence flexible) suspensions require a large chip area. It is shown in Section 3 that a resolution of milli-g to several gs can be achieved by most fabrication processes within a chip area of 500 μm × 500 μm. Most capacitive micro-g resolution accelerometers occupy an area of at least 1 mm × 1 mm.

To improve the dynamic behavior of high-resolution accelerometers, they are operated in the force re-balance mode (i.e., in the closed loop mode), wherein the output voltage is applied as a feedback force to the accelerometer proof-mass in a direction opposite to that of the applied acceleration[36]. Some compensators or proportional-integral-derivative (PID) controllers are used in the feedback path to make this system stable[37]. The closed-loop mode improves the bandwidth, linearity, and range of the accelerometer, however, the sensitivity and resolution decrease. These and various other implementation aspects of closed-loop operation are detailed in Section 4.

used to cancel the offsets and noise signals. For high-resolution accelerometers, usually capacitive sensing techniques are used because of their advantages such as high sensitivity, low temperature-dependence, low drift, and amenability for feedback[35]. The basic working principle of the mechanical components and the principle of capacitance detection are

Figure 3: Resolution Vs. sensitivity of some commercial micromachined accelerometers. FSC = Freescale semiconductors, C = Colybris, CB = Crossbow, ST = ST Microelectronics, and AD = Analog devices. The data shown is based on the specifications published by the respective companies at the time of this publication.
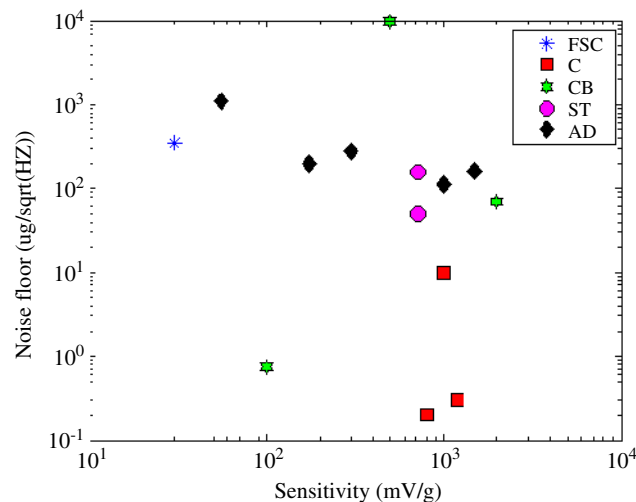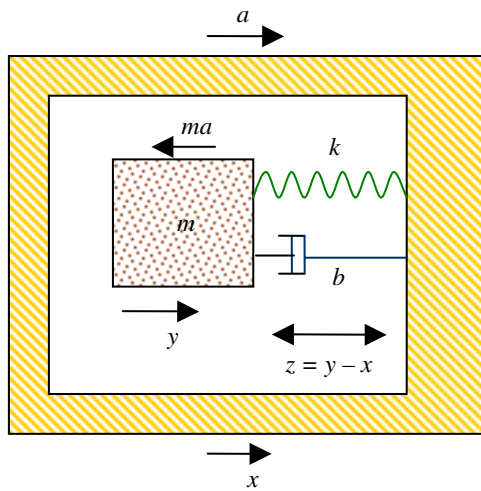
Figure 4: Principle of operation of an accelerometer.

One of the major aspects of achieving high mechanical sensitivities is the ability of the fabrication process to form a bulky proof-mass to increase the force and sufficiently thin and narrow suspension beams to reduce the stiffness. Both of these help increase the measured displacement of the proof-mass. The mechanical components of the accelerometers are fabricated by either surface or bulk micromachining. Surface micromachining[38] gives very fine feature sizes, but thin proof-mass, whereas bulk micromachining[22] gives huge wafer-thick proof-mass but also thick suspensions. The evolution of the fabrication process towards a combination of both surface and bulk micromachining processes to get thick proof-mass and compliant suspensions[14] is described in Section 5.

The resolution of accelerometers is mainly limited by the noise and the offsets in the electronic circuitry. Capacitance detection circuitries differ from each other in the manner in which they cancel these offsets and reduce the noise levels. A number of analog and digital techniques are reviewed in Section 6. Section 7 summarizes the main points of the paper and discusses further opportunities for improving the resolution of micromachined accelerometers.

In the next section, we present the basic working principles of mechanical and electronic components of micromachined accelerometers.

2. Working Principles of High-resolution Accelerometers

2.1. *Mechanical components*

For acceleration to be sensed, most accelerometers convert the effect of acceleration to displacement and then transduce it to a voltage so that it can be signal-conditioned and worked upon further. As noted earlier, accelerometers have a proof-mass, which experiences an inertial force in the opposite direction of the acceleration that is to be measured. The deflection of the proof-mass caused by this force is determined by the suspension's stiffness and is converted to a voltage using a suitable principle of transduction (see Table 1). For frequencies of the input acceleration that are sufficiently smaller than the natural frequency of the device, the deflection is linear with the acceleration.

A lumped spring–mass–damper (k–m–b) model schematically represents an accelerometer as shown in Fig. 4. The acceleration of the frame (a), which is to be sensed, manifests as the inertial force (ma) on the mass. The equations below show the derivation of the sensitivity of the accelerometer using the fundamentals of mechanics and vibration theory[39].

The movement of the frame is denoted by x and that of the mass by y. The net extension of the spring and the damper will thus be $z = y - x$. The equation of motion, by summing the forces—inertial, damping, and spring forces—to zero, is then given by:

$$m\ddot{y} + b(\dot{y} - \dot{x}) + k(y - x) = 0 \qquad (1)$$

By substituting $z = y - x$ and assuming that frame's excitation is harmonic, $x = X \sin \omega t$ with amplitude, X, and frequency, ω, Eq. (1) can be re-written as follows.

$$m(\ddot{z} + \ddot{x}) + b\dot{z} + kz = 0$$
$$\Rightarrow m\ddot{z} + b\dot{z} + kz = -m\ddot{x} = m\omega^2 X \sin \omega t \quad (2)$$

By denoting the amplitude of z as Z, Eq. (2) can be solved to obtain the following result.

$$\frac{Z}{X} = \frac{m\omega^2}{\sqrt{(k - m\omega^2)^2 + (b\omega)^2}} \qquad (3)$$

Now, by defining terms of the form $\omega_n^2 = \frac{k}{m}$ and $\xi = \frac{b}{b_c}$ where $b_c = \sqrt{4km}$, we recast Eq. (3) as

$$\frac{Z}{X} = \frac{\frac{\omega^2}{\omega_n^2}}{\sqrt{(1 - \frac{\omega^2}{\omega_n^2})^2 + (2\xi \frac{\omega}{\omega_n})^2}} \qquad (4)$$

When operated at frequencies much less than the resonance frequency, i.e., when $\omega \ll \omega_n$, the denominator approaches unity. We then get $Z = \omega^2 X / \omega_n^2$. But $\omega^2 X = a$ (equal to the acceleration) gives:

$$Z = \frac{a}{\omega_n^2} \qquad (5)$$

Table 1: Various types of accelerometers and their sensing techniques

Type of sensing, Range of sensing, and Description	Applications	Advantages	Shortcomings
1) Piezo-resistive (0.001-50 g)[20,21] Bending of suspension beams due to proof-mass displacement produces strain in them. This is measured as a change in the resistance of a piezoresistor placed at the support end of the beam. Change in resistance is measured by using a Wheatstone bridge configuration.	Air bag deployment in automobiles; High-g accelerometers used for impact testing etc.	a) Simplicity in structure and fabrication. b) Simple readout circuitry generating a low-impedance voltage.	a) Large temperature sensitivity. b) Small overall sensitivity of 1–2 mV/g and thus requires a huge proof-mass.
2) Capacitive (2μg- several gs)[22] Displacement of a mass due to applied acceleration leads to a change in capacitance between two plates, one fixed and the other one attached to the moving mass. The capacitance change can be due to a change in the overlapping area or due to a change in the gap.	Air bag deployment in automobiles, Inertial navigation, micro gravity detection, etc.	High sensitivity, good dc response, good noise performance, low drift, low power dissipation, low temperature sensitivity, amenability for feedback.	Parasitic capacitance, electromagnetic interference.
3) Tunneling (10 ng- 5 g)[15,16,25−29] This accelerometer consists of a proof-mass with a sharp tip separated from a bottom electrode. As the tip is brought sufficiently close to its counter-electrode (within a few Å) a tunneling current is established. This tunneling current is used as a measure for acceleration. This is operated in the closed-loop mode.	Inertial navigation, micro-gravity measurement in space.	High sensitivity, excellent resolution, linearity can be maintained by operating in the closed-loop mode.	Difficult to fabricate sharp tips; nonlinear variation of tunneling current with distance; high noise levels.
4) Piezoelectric (High g)[23] In this type, the sensing element is a crystal, which has the p roperty of creating a charge when subjected to mechanical strain. In the accelerometer, this crystal is bonded to a mass such that when the accelerometer is subjected to the inertial force, the mass strains the crystal that emits a signal. This signal is related to the imposed 'g' force.	Vibration sensors; active vibration control.	High bandwidth; simple in operation and can be incorporated in any application; amenable for actuation and thus vibration control.	Low resolution, low sensitivity, and high voltage requirements.
5) Optical (Nano-g to high g)[11,12,30] When light from a Light emitting Diode (LED) source is projected onto a moving membrane, the reflected light from it has a lower intensity. The intensity loss is a measure of the acceleration. Similarly, a change in wavelength, polarization as well as diffraction could be used.	Inertial navigation, detecting small vibrations in machines.	High resolution, low noise, can operate in places where other principles fail (e.g., when electromagnetic fields are present).	Large weight, complex fabrication process and detection circuitry.
6) Resonant (5 − 5000 g)[31,32] This type of acceleration measurement makes use of the shift in the natural frequency of the structure with applied acceleration.	Vibration sensors in machine tools.	High dynamic range, sensitivity, bandwidth, adaptable to digital circuits.	Leakage of signal, high noise levels.
7) Thermal (0.5 mg to high g)[33] It consists of a substrate which is sealed with air or any other gas with a heater exactly in the middle. Two thermocouples are present at the ends of the substrate. When the acceleration is applied, the hot air around the heater is pushed to one of the ends by denser cold air thus giving a temperature difference in the thermocouples which is proportional to the acceleration.	Inclination sensing (Dual axis), automotive, electronic and gaming applications.	Low cost, low noise, less drift, simple signal conditioning circuitry.	Low resolution, batch fabrication can be difficult, temperature-sensitivity, etc.
8) Electromagnetic (0-50 g)[24] It consists of two coils, one on the proof-mass and the other on the substrate. A square pulse is given to the primary and a voltage is induced in the secondary, which is proportional to the distance between the proof-mass and the substrate	Air bag deployment.	Good linearity, simple signal conditioning.	High power, low resolution, low sensitivity.

By observing the above formulae, it is evident that the natural frequency has to be low for high sensitivity. But this has the side-effect of reducing the bandwidth, which is dependent on both the fundamental frequency and the damping factor. This is shown in Fig. 5 where the frequency response is schematically illustrated. For under- or over-damped situations, the amplitude ratio remains constant for shorter range of frequencies than the critically damped frequency. Thus, the greater the sharpness at resonance the greater the available operating range for the frequency of the accelerometer (see Fig. 5). The sharpness at resonance is quantified by the quality factor, $Q = 0.5/\xi$. However, the under-damped conditions result in a ringing response, where the transients do not die down quickly. Thus, most accelerometers are operated at critical damping conditions[36] so

Figure 5: The frequency response curve of an accelerometer[18].
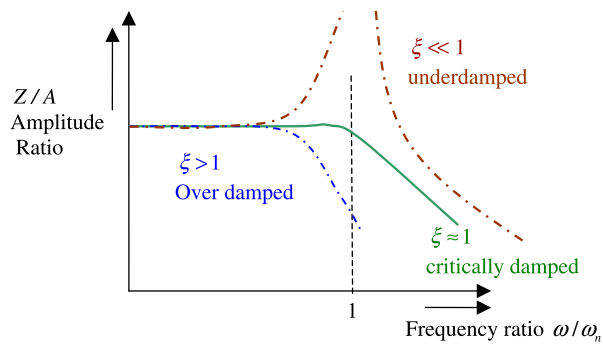
as to have a high bandwidth and good sensitivity. Closed-loop operation, which will be discussed in detail in Section 4, makes it possible to have underdamped or even vacuum-packaged accelerometers (i.e., extremely low damping) but the problems associated with transients need to be dealt with carefully.

The displacement of the proof-mass is transduced into an electrical quantity (e.g., capacitance in capacitive accelerometers). The size of the proof-mass and the stiffness and damping of the suspension decide the sensitivity, which is the change in capacitance per unit acceleration. The resolution depends on the noise, both mechanical and electronic, in the system. Figure 6 shows the noise floor against the bandwidth of different types of accelerometers. Of the various sensing techniques summarized in Table 1, only capacitive, tunneling, and interferometric methods give high sensitivity and fine resolution. The dashed orange line is the best linear fit to the data. The solid magenta line is based on a metric defined to be the ratio of the noise floor and the bandwidth raised to 1.5 (i.e., $a_{nf}/BW^{3/2}$) that can be used to

Figure 6: A plot of the accelerometer noise with the sensor natural frequency. While the performance of most of these accelerometers, which were demonstrated in research labs, nicely align with the theoretical relationship (the solid line with a slope of 1.5), the commercial ones shown in Fig. 3 do not This implies that many factors such as packaging and environment significantly affect the performance. (Note: the two commercial ones shown here (ADXL05, 105) do lie close to the line).
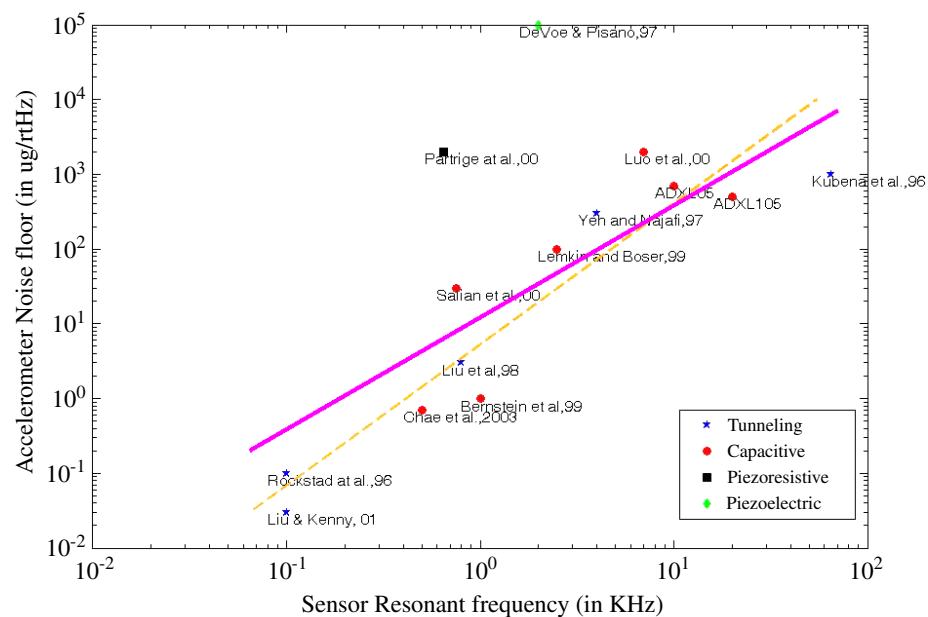
Figure 7: Differential Capacitance arrangement (a) differential capacitance arrangement in for an out of plane Z-axis accelerometer, (b) Differential capacitance arrangement for an in-plane accelerometer with positive and negative static electrode along the same side of the proof-mass, (c) for the in-plane accelerometer with positive and negative electrodes on either side of the proof-mass.
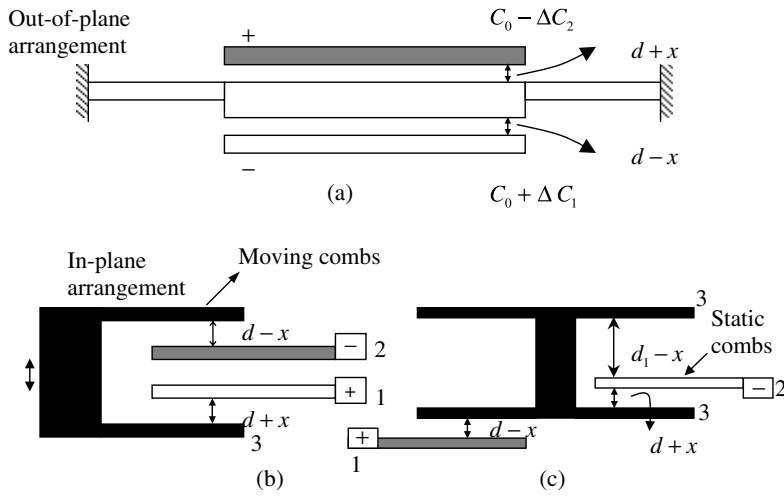
compare different accelerometers. The rationale for this metric can be understood from Eq. 5, which shows the amplitude of the proof-mass motion as the ratio of the acceleration signal to the square of the natural frequency. This means that, we can obtain the amplitude of motion (and hence the ensuing electrical signal) for the minimum resolvable acceleration, a_r.

$$Z_{\min} = \frac{a_r}{\omega_n^2} \simeq \frac{a_r}{BW^2} \simeq \frac{a_{nf}\sqrt{BW}}{BW^2} = \frac{a_{nf}}{BW^{3/2}} \quad (6)$$

This metric has a slope of 1.5 in the log-log plot shown in Fig. 6. Furthermore, the lower the metric the better the accelerometer. Next, we briefly describe the three transduction principles.

2.2. *Capacitance detection*

The deflection of the proof-mass is converted to a change in capacitance. This is usually done with a differential capacitance arrangement as it gives high sensitivity and good linearity. Many other arrangements are possible[40]. In the differential capacitance arrangement, the electrode attached to the proof-mass moves between two other static electrodes of opposite polarity. Figure 7a shows a z-axis accelerometer, where the proof-mass acts as the moving electrode with two static electrodes above and below it.

In-plane accelerometers usually use comb-fingers (see Fig. 7b-c), which protrude from the proof-mass to measure capacitance-change. Two kinds of arrangements for these comb-drives are explored here.

Type 1: In the first arrangement, as shown in Fig. 7b, the two static electrodes of opposite polarity are situated along the same side of the proof-mass[41]. In this arrangement, alternative static combs, which are of opposite polarity (i.e., 1 and 2), need to be isolated from each other to prevent shorting. Isolating these combs may not be possible in most fabrication processes because a number of connections need to cross one another as shown in Fig. 8a.

Type 2: In this type (see Fig. 7c), the stationary negative combs are connected on the one side and the positive combs on the other[42]. This means that two combs on either side make one differential capacitance arrangement. There will be some parasitic capacitance between the moving electrode and the static electrodes marked 1 and 2 in Fig. 7c. There is a loss in sensitivity due to this type of arrangement, which is explained later in this sub-section. The advantage here is that the positive and the negative static electrodes are connected together as shown in Fig. 8b without having to interweave with each other.

The change in capacitance between the moving combs and the two static electrodes is measured as an voltage-change. The circuit diagram to measure this voltage-change is shown in Fig. 9 [40]. The two variable capacitors indicated in the figure are the capacitances between the static and the moving combs.

High-frequency pulses V of opposite phases are applied to nodes 1 and 2 as shown in Fig. 9. This

means that in any cycle, if the voltage at node 1 is V, the voltage of node 2 is $-V$. The output is taken at node 3. This output voltage is given by

$$V_{out} = V - \frac{(C_0 - \Delta C_2)\,2V}{2C_0 - \Delta C_2 + \Delta C_1} \qquad (7)$$

which simplifies to

$$V_{out} = \frac{(\Delta C_1 + \Delta C_2)}{2C_0 - \Delta C_1 + \Delta C_2}V \approx \frac{\Delta C_1 + \Delta C_2}{2C_0}V$$

$$= \frac{\Delta C_1 + \Delta C_2}{C_s}V \text{ for } \Delta C_1 - \Delta C_2 \ll 2C_0 \quad (8)$$

where $C_s = 2C_0$ is the sense capacitance.

Changes in capacitance ΔC_1 and ΔC_2 are obtained by change in the distance between the electrodes d. Referring to Fig. 7b, the output voltage is given by

$$V_{out} = \frac{\dfrac{\varepsilon_0 A_p}{d-x} - \dfrac{\varepsilon_0 A_p}{d+x}}{\dfrac{2\varepsilon_0 A_p}{d}}V$$

$$= \frac{xd}{d^2 - x^2}V \approx \frac{x}{d}V \text{ for } x \ll d \qquad (9)$$

where A_p is the area of overlap between the electrodes and ε_0 is the permittivity of air.

$$\Delta C = \Delta C_1 - \Delta C_2 = \frac{\varepsilon_0 A_p}{d-x} - \frac{\varepsilon_0 A_p}{d+x}$$

$$= \frac{\varepsilon_0 A_p}{d}\left(\frac{\frac{2x}{d}}{1-\left(\frac{x}{d}\right)^2}\right) = C_0\frac{\left(\frac{x}{d}\right)}{1-\left(\frac{x}{d}\right)^2} \quad (10a)$$

For small displacements, i.e., when $x \ll d$, we get

$$\Delta C = C_0\frac{\left(\frac{x}{d}\right)}{1-\left(\frac{x}{d}\right)^2} \approx C_0\frac{x}{d} \Rightarrow \left(\frac{\Delta C}{C_0}\right)_a = \frac{x}{d}$$

$$(10b)$$

In the case of Fig. 7c, the change in capacitance is given by

$$\Delta C = \frac{\varepsilon_0 A_p}{d-x} - \frac{\varepsilon_0 A_p}{d_1-x} - \frac{\varepsilon_0 A_p}{d+x} + \frac{\varepsilon_0 A_p}{d_1+x}$$

$$= C_0\frac{\left(\frac{x}{d}\right)}{1-\left(\frac{x}{d}\right)^2} - C_1\frac{\left(\frac{x}{d_1}\right)}{1-\left(\frac{x}{d_1}\right)^2} \quad (11a)$$

For small displacements, i.e. $x \ll d$, we get

$$C_0\frac{\left(\frac{x}{d}\right)}{1-\left(\frac{x}{d}\right)^2} - C_1\frac{\left(\frac{x}{d_1}\right)}{1-\left(\frac{x}{d_1}\right)^2} \approx C_0\frac{x}{d} - C_1\frac{x}{d_1}$$

$$(11b)$$

where $C_0 = 2\varepsilon_0 A_p/d$ is the base capacitance between a pair of combs. The expression $C_1 = 2\varepsilon_0 A_p/d_1$ is the capacitance between the stationary comb of one pair and the moving comb of the other pair, which can be termed as the cross-capacitance. The ratio of the change in capacitance of this type to the base capacitance can then be given as

$$\left(\frac{\Delta C}{C_0}\right)_b = \frac{C_0\frac{x}{d} - C_1\frac{x}{d_1}}{C_1 + C_2} = x\frac{\left(\frac{1}{d_1}\right)^2 - \left(\frac{1}{d}\right)^2}{\frac{1}{d_1} + \frac{1}{d}}$$

$$= \frac{x(d_1 - d)}{d_1 d} \qquad (12)$$

So, by comparing the two types of sensing, the ratio of the fractional change in capacitance in type 2 to that of type 1 is given by

$$r_{a/b} = \frac{(\Delta C/C_0)_b}{(\Delta C/C_0)_a} = \frac{d_1 - d}{d_1}$$

by taking

$$\frac{d_1}{d} = \alpha, \quad r_{a/b} = 1 - \frac{1}{\alpha} \qquad (13)$$

Figure 8: Arrangement of the differential capacitance configurations (a) for the type 1 arrangement with positive and negative static electrodes on the same side of the proof-mass (b) type 2 arrangement where the positive and the negative electrodes are on either side of the proof-mass.
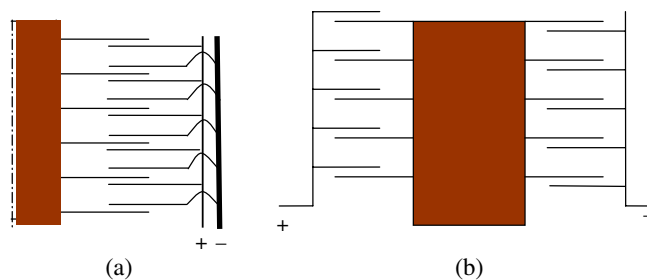
(a)   (b)

Figure 9: Circuit diagram to measure the differential capacitance change.
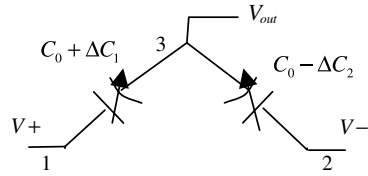
From Eq. 13, it can be seen that for a large value of α, the loss in sensitivity for type 2 is minimized. In both cases, if the sensing distance d is reduced, the sensitivity of the accelerometer increases. This is evident from Eq. 10b. However, a small sense gap warrants a tight tolerance in the fabrication process, which is usually hard to achieve. This is further elaborated in Section 5.

2.3. *Tunneling principle*

The tunneling principle is one of the most sensitive of all the available transduction principles for converting the displacement to voltage. It consists of two electrodes separated by a very small distance d. When a bias voltage V_b is given between the electrode plates, there is a current flowing between them, which is given by[25]

$$I \propto V_b e^{(-\alpha d \sqrt{\phi_s})} \qquad (14)$$

where $\alpha = 1.025 (\text{Å})^{-1} \text{eV}^{-1/2}$, ϕ_s is the work potential between the two surfaces through which tunneling takes place. The current increases by an order of magnitude for a change corresponding to 1 Å displacement[25]. Using this principle for accelerometers, the moving electrode is attached to a proof-mass, while the static electrode is kept beneath it. For tunneling to be effective, the moving electrode has to have a very sharp tunneling tip as shown in Fig. 10. A number of tunneling accelerometers are presented in the literature[25–29]. These accelerometers are sensitive and have a low noise floor. But they are also extremely difficult to fabricate because they require a sharp conducting tip. Furthermore, there is a chance of the tunneling tip to wear out if there is a constant or intermittent contact. To overcome this, tunneling accelerometers are operated in the force re-balance mode. This is illustrated for capacitive accelerometers in later sections.

2.4. *Interferometric principle*

The optical interferometric principle gives a displacement resolution that matches that of the tunneling method[11,12]. In this, a pair of interdigitated comb fingers is attached to the fixed substrate and the moving proof-mass; one set to the substrate and the other to the proof-mass. When the suspension-restrained proof-mass moves up and down, one set of fingers move along with it. The laser light that falls on the fingers then creates a diffraction pattern, whose intensity is measured and calibrated for acceleration. This is pictorially shown in Fig. 11. Some are of the the Michelson type[43] and the others Fabry–Pérot cavity type[11,12]. In one embodiment of the latter type, a laser diode and photo detector were integrated along with the micromachined chip in an acrylic package of 8.6 cm^3 volume. Because the intensity of the diffracted light varies linearly with the relative motion between the stationary and moving fingers, this accelerometer can be operated in the open-loop mode. This simplifies the control and electronic circuitry. However, the size is not in favor of this type of accelerometer. But opportunities do exist for miniaturization[12].

3. Noise sources in accelerometers

Noise in accelerometers occurs due to the mechanical components as well as the electronic components. The white-noise floor is expressed in terms of the spectral densities of the noise signal, which is constant for all frequencies[40]. The actual noise which limits the resolution of the system thus depends upon its spectral density and the range of the operating frequencies, i.e., the bandwidth of the system. The spectral density d_{sp} of the noise-floor at the output of the accelerometer is expressed in $V/\sqrt{\text{Hz}}$. If BW denotes the bandwidth of the accelerometer in Hz, then the rms value of the noise floor is given by[44]

$$V_{rms} = d_{sp} \times \sqrt{BW \times c} \qquad (15)$$

where c is a number chosen based on experience*. Therefore, for a large bandwidth, the minimum detectable signal is large. This limits the resolution for a given noise-floor. It can be seen from Fig. 6

---

*Analog Devices Inc. recommends 1.6 for c.

that the noise-floor is low for devices with low bandwidth. This relationship is evident from the concentration of the previously published accelerometers along the dashed orange line in the log-log plot. If the bandwidth of the system is small, then the resolution of the device improves. This means that the devices with very low bandwidth would be able to resolve minute changes in acceleration better than those with large bandwidth. However, this is not consistently true with the commercial accelerometers shown in Fig. 3. Possible reasons for this might be that packaging and environmental factors are different and the reported values of noise floor might not be applicable for the full range of the bandwidth in all cases. There are also other sources of noise as explained ahead.

3.1. *Mechanical noise*

To probe the possible noise sources in a mechanical system, we make use of the Fluctuation-Dissipation theorem[46], which states that if there is a mechanism for dissipation in a system, then there will also be a component of fluctuation directly related to the dissipation. This is because any random motion generated within the system decays if there is an energy dissipating mechanism. This might lead to the temperature of the system becoming less than that of the surroundings. To account for this, there is an associated fluctuating force. This force acts as noise. In a spring–mass–damper model (see Fig. 12), the energy is dissipated through the damper and hence there should be a component of the force at the input due to fluctuations.

Fluctuation-dissipation theorem: Any dissipative process has fluctuations even in equilibrium. For example, an electrical resistor has a fluctuating voltage across its terminals even when it does not carry any current. Similarly, a constrained mass vibrates in the absence of a force. The fluctuation-dissipation theorem states that the response of thermodynamic system in equilibrium for a perturbation is the same as that due to a fluctuating force.

Nyquist relation: Nyquist relation gives the value of the fluctuating force on a dissipative mechanical system in equilibrium in terms of damping and temperature. It is the mechanical analogue of the Johnson's noise found in electrical resistors.

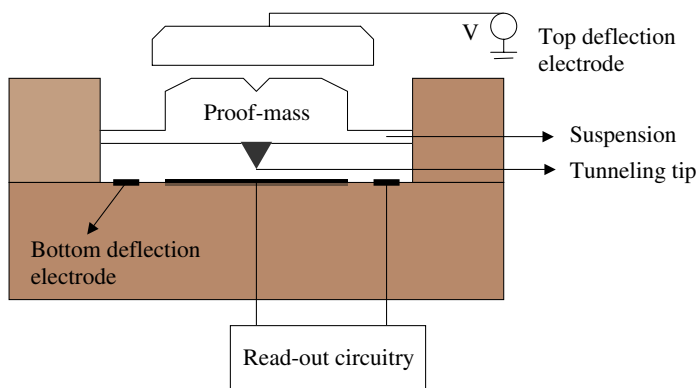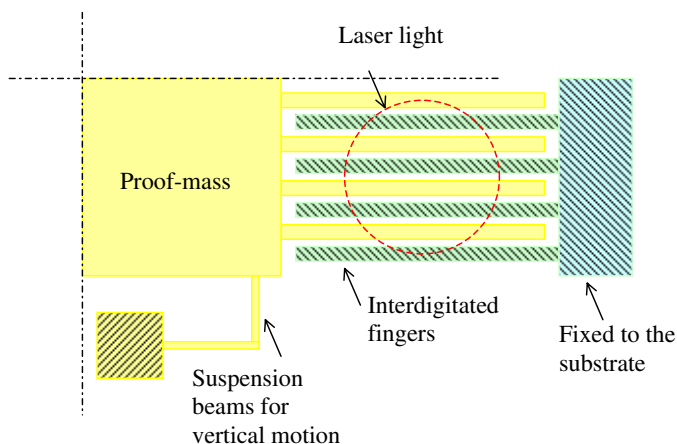Figure 10: Working principle of a tunneling accelerometer[25].

Figure 11: Schematic illustration of a quarter of the micromachined Fabry–Pérot type interferometric accelerometer[12]. The interdigitated fingers (shown in different colors) attached to the vertically movable proof-mass are exposed to laser light. In the presence of acceleration, when the movable fingers displace to a different height, the diffracted light intensity changes linearly with acceleration.

By using the Nyquist relation, we can determine the spectral densities of the fluctuating force as shown below.[46]

$$F_f = \sqrt{4K_B bT}$$

where

$$
\begin{aligned}
F_f &= \text{Fluctuating force in N/}\sqrt{\text{Hz}} \\
K_B &= \text{Boltzmann's constant in N–m/K} \quad (16)\\
b &= \text{Damping coefficient in N–s/m} \\
T &= \text{absolute temperature in K}
\end{aligned}
$$

Thus, any complex mechanical system can be analyzed for thermo-mechanical noise by adding a force-generator along with a damper. If the frequency components in the noise signal are within the operating range, then we can express the displacement of the mass as follows.

$$X_n = \frac{\sqrt{4K_B bT}}{k} \text{ in m / }\sqrt{\text{Hz}} \qquad (17)$$

The detected displacement of the proof-mass due to a signal expressed in the spectral density form, can be given by

$$X_s = \frac{A_s}{\omega_0^2} \text{ in m / }\sqrt{\text{Hz}} \qquad (18)$$

Where A_s is the amplitude of the spectral density of the acceleration noise-floor. Now, the signal-to-noise ratio (SNR) is as shown below.

$$
SNR = \left(\frac{X_s}{X_n}\right)^2 = \frac{k^2 A_s^2}{4K_B bT\omega_0^4} = \frac{M^2 A_s^2}{4K_B bT}
$$

$$
= \frac{MA_s^2}{4K_B T\omega_0}\left(\frac{M\omega_0}{b}\right) = \frac{MA_s^2 Q}{4K_B T\omega_0} \quad (19)
$$

From the above equations, it can be inferred that increasing the mass and the quality factor along with decreasing the natural frequency can reduce the noise considerably. But this limits the bandwidth of the system. In general we can conclude that increasing the sensitivity as well as decreasing the noise in an accelerometer involves decreasing the natural frequency, thus limiting the range of operating frequencies.

3.2. *Electronic noise sources*

The main source of electronic noise is due to the amplifier used to amplify the signal obtained from the differential capacitance setup. An amplifier has a number of stages of amplification. Thus, the noise in the first stage is amplified in the successive stages of the op-amp[40]. This noise is mainly limited by the Johnson's noise due to resistors in the circuitry. Another equally important noise source is the $1/f$ or the flicker noise. This is predominant in low frequency signals and occurs due to trapping and subsequent release of electrons along the semiconductor[40]–oxide interface in circuits implemented using CMOS technology. The front-end amplifier thermal noise spectral density is given by

$$S_{n-amp} = 4k_B T\left(\frac{2}{3g_m}\right)(1+F_n) \qquad (20)$$

where, g_m is the transistor transconductance at the operating point of the op-amp, and F_n the noise factor. The $1/f$ noise is given by

$$S_{n-1/f} = \frac{K_f}{WLC_{ox}f} \qquad (21)$$

where, K_f is a scale factor, WLC_{ox} is the gate-to-channel capacitance. These terms are well defined in a book by Senturia[40]. In digital circuits, there is an additional noise. This is called the quantization noise[6]. It is given by

$$n_{rms} = e_{rms}\frac{\pi^2}{\sqrt{5}M^{2.5}} \qquad (22)$$

Figure 12: Lumped characterization of the mechanical noise.
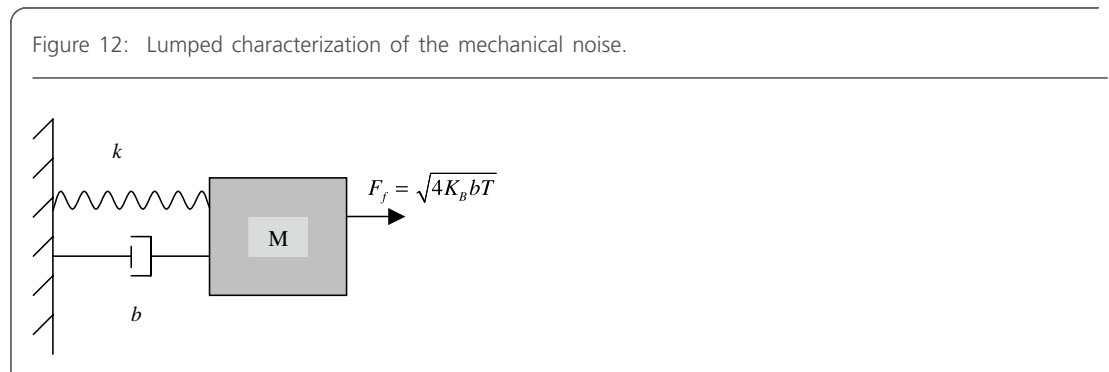
Figure 13: Block diagram of the capacitive detection circuit including mechanical and electronic noise sources.

where e_{rms} is the unshaped value of the quantization noise for a $\Sigma - \Delta$ converter and M is the oversampling ratio[13]. These are elaborated in Section 6.

Kulah et al.[13] showed that the electronic noise ($\approx 2\mu g/\sqrt{Hz}$) dominates when compared to the mechanical noise ($\approx 0.5 \mu g/\sqrt{Hz}$). This means that the mechanical signal should be more sensitive than the electronic noise floor for smal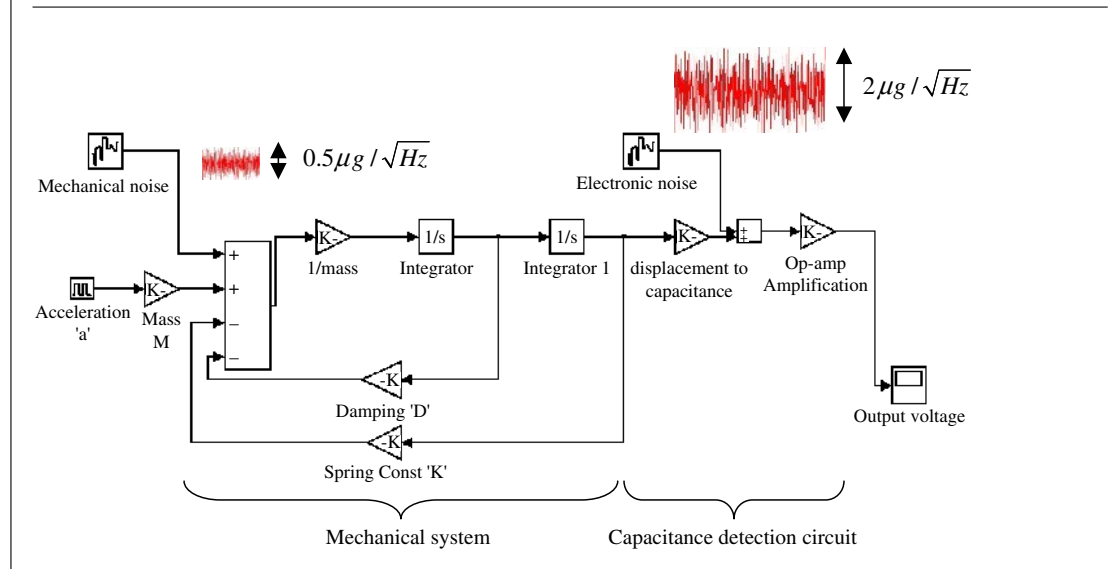l changes in acceleration to be detected. Kulah et al.[13] also note two other sources of noise. The first is the Source Charging Reference Voltage (SCRV) noise. This occurs due to the noise in the reference voltage that is used to charge the sense capacitor in each cycle. This becomes dominant at high sampling frequencies. The second is the residual motion of the proof-mass in the closed-loop operation. Here, the proof-mass will not be completely stationary in the changing acceleration environment. This contributes to additional noise in the measurement circuitry. This noise is inversely proportional to the square of the frequency. Hence, it is dominant at the low frequencies. This is attributed to decreased resolution in the closed-loop mode as compared with the open-loop resolution[13].

3.3. *Achieving μ-g resolution: an example*

It is now clear that the resolution of the accelerometer is limited by the mechanical and electronic noise sources. This means that the smallest signal that can be detected would have to be greater than the noise floor in the circuit. These two noise sources can be included in the circuit model of the accelerometer system as shown in Fig. 13. For

most capacitive detection circuits, a resolution of 1 part per million can be safely assumed. This means that if the base capacitance is C_0, a capacitance change 10^{-6} can be detected. However, there are some capacitance detection circuits, which can detect a minute capacitance change as low as 10 aF. Furthermore, the sense-capacitance C_0 should be more than the parasitic capacitance in the circuit, which is usually around 0.5 pF. For detecting 1 μg acceleration, these constraints can be represented as follows.

$$\frac{\Delta C}{C_0} \approx \frac{x}{d} > 1e - 6 \qquad (23)$$

For a sense-gap of around 1.5 μm [27], the deflection required for the proof-mass of the accelerometer is around 1.5×10^{-6} μm. A proof-mass of size 2.4 mm $\times$ 1 mm, with a suspension stiffness of 17 N/m [27] is able to give a displacement of 1.2×10^{-6} μm, which promises μg resolution. The overall chip-area of such an accelerometer is around 3 mm $\times$ 2 mm. The proof-mass thickness is 460 μm. If the area is reduced to 1 mm $\times$ 1mm, the resolution, with the same electronic circuitry falls to 16 μg. With a 500 μm area, the minimum acceleration that can be detected is around 400μg. Thus, we can see that a large chip area is needed to make the mechanical components sufficiently sensitive.

It is further seen from the above analysis that the maximum detectable acceleration is less than 1 *g* because, at this acceleration, the moving electrode comes into contact with one of the static electrodes. Furthermore, a large proof-mass and a flexible suspension reduce the natural frequency and thus

the bandwidth of the accelerometer. To circumvent these problems, these accelerometers are operated in force re-balance (closed-loop) mode. This is described in detail in the next section.

4. Closed-loop Operation

High-resolution accelerometers are usually operated in the closed-loop mode to increase their bandwidth and the range of operation. In this mode, the output voltage of the capacitance detection circuit is fed back to the proof-mass and an electrostatic force in a direction opposite to that of the acceleration is applied[14]. In other sensing modes, a suitable actuation is necessary for providing the feedback. The feedback ensures that the deflection of the proof-mass is very small and thus it increases the range of operation. Additionally, the minute proof-mass movement improves the linearity of the system. Feedback improves the bandwidth by a factor equal to loop gain[45]. Furthermore, feedback improves the dynamic range, drift, and temperature sensitivity. Sensitivity of an open-loop accelerometer is inversely proportional to the spring constant of its suspension which in turn is proportional to the cube of the length as well as the thickness of suspension beams. So, a small change in processing causes a large change in the sensitivity. By operating sensing element in electronic force feedback loop, strong dependence of accelerometer on processing parameters can be reduced substantially[47]. However, operating in the closed-loop mode may make the system unstable for large feedback gains. There might also be a decrease in the sensitivity of the system. In this section, we study the effects of some controllers used for feedback, their effect on the bandwidth, sensitivity, and the stability of the system.

Figure 14 shows a block diagram of the of a closed-loop accelerometer, where each block depicts a state-space transfer function of the various components of the accelerometer. The mechanical component is represented by a second order transfer function, while the amplifier and the modulation are represented by simple gains in the circuit (K_a and K_v respectively). The feedback is represented by a gain K_{fb}.

If the feedback was just a gain factor $K_{fb} = K$, the closed-loop transfer function of the accelerometer becomes

$$TF_k = \frac{V(s)}{A(s)} = \frac{mK_vK_aK}{ms^2 + ds + k + K_vK_aK} \quad (24)$$

By substituting $s = 0$ in Eq. (24), it can be seen that a simple proportional feedback has a steady-state error associated with it. With a large feedback gain, the system response tends to oscillate

as it moves farther away from the real axis, thus decreasing the system's damping.

By using a controller with an extra pole along the feedback path, i.e., by having $K_{fb} = K/(1 + \tau s)$, we get an additional degree of freedom in designing the circuit. However, it can be seen from the transfer function below that the steady state error is still not overcome. The farther the electronic pole from the origin $(-1/\tau)$ the better the bandwidth and the dynamic behavior of the system[40].

$$TF_k = \frac{V(s)}{A(s)} = \frac{mK_vK_aK}{(ms^2 + ds + k)(1 + \tau s) + K_vK_aK} \quad (25)$$

To overcome the problem of the steady-state error, a PID controller of the form $K_{fb} = K(1 + \beta/s + \gamma s)$[37] is used. The closed-loop transfer function of the system is then given as follows.

$$TF_k = \frac{V(s)}{A(s)}$$
$$= \frac{mK_vK_aK(s + \beta + \gamma s^2)}{(ms^2 + ds + k)s + K_vK_aK(s + \beta + \gamma s^2)} \quad (26)$$

The integral term β helps reduce the steady state error. But increase in its value leads to oscillations. The differential term γ helps reduce the ringing response of the system. A value of $\beta \approx 100\gamma$ is chosen for good system response. The PID controller is widely used in most closed-loop accelerometer circuits. In the above analysis, it is assumed that the amplifier is ideal and there is no noise in the system. However, in reality, the amplifier will have some bandwidth of its own and the noise in the circuit does affect the closed-loop response of the system[40]. It is further seen that the closed-loop noise floor is more than the open-loop noise floor[13]. In practice, it is seen that the closed-loop noise floor is sometimes ten times more than that of the open-loop noise floor. The authors attribute this to the environmental factors[13]. This issue needs further investigation.

4.1. Feedback to the proof-mass

The proof-mass is subjected to a feedback force by applying the output voltage of the electronic circuit to a set of feedback combs. However, it is to be noted that the forces produced by the voltage applied between two electrodes is always attractive in nature. Assuming an area of overlap of A and a sense gap of d, the electrostatic force between two electrodes is given by

$$F_{el} = \frac{\varepsilon_o A V^2}{d^2} \quad (27)$$

Figure 14: Mathematical model of the analog closed-loop accelerometer.
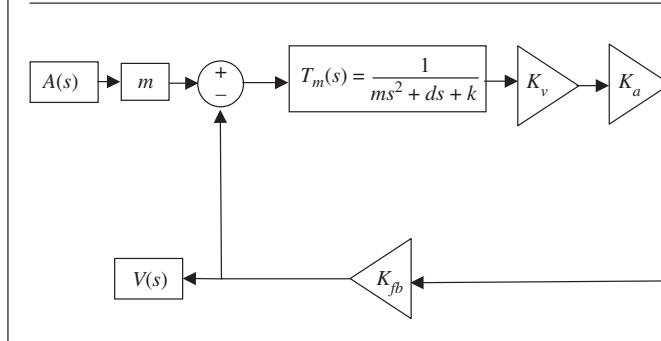
It can be seen from the above equation that the electrostatic force varies nonlinearly with the applied voltage. To linearize the force vs. voltage relationship, the arrangement shown in Fig. 15 is used[34,36]. Here, a dc bias is applied to two static combs so that the net force on the moving comb is zero. The feedback voltage is then added to the dc bias on one comb and subtracted from it in the other comb.

The feedback force is given by

$$F_{fb} = \frac{\varepsilon_0 A n_{fb} (V_b + V_{fb})^2}{2(d-x)^2} - \frac{\varepsilon_0 A n_{fb} (V_b - V_{fb})^2}{2(d+x)^2}.$$
(28)

By assuming $d \gg x$, Eq. 28 can be simplified as follows.

$$F_{fb} = \frac{2\varepsilon_0 n_{fb} A V_b V_{fb}}{d^2}$$
(29)

where n_{fb} is the number of feedback combs. It can be seen from Eq. 29 that the feedback force is proportional to the voltage V_{fb}. It is further seen from Eq. 28 that the maximum value of the feedback voltage V_{fb} is the bias voltage V_b. This is because the second term of the right-hand side of the equation becomes zero at this voltage. This determines the operating range of the accelerometer. Care should be taken to see that the dc bias V_b is far from the pull-in voltage of the structure. Since, the maximum voltage applied on combs (as seen from the left set of feedback combs in Fig. 15, when $V_{fb} = V_b$) is

$2V_b$, the bias voltage V_b should be less than half the pull-in voltage.

In the first four sections, we have outlined the basic components of the high-resolution accelerometers. In the next section, we describe the evolutionary development of the accelerometers towards achieving inertial grade resolution by considering representative examples from the literature.

5. Evolution of high-resolution, high-sensitivity accelerometers

It was mentioned in the previous section that high-resolution accelerometers require a large proof mass and flexible suspensions, which in turn depend on the effectiveness of the fabrication processes. We chronologically illustrate the developments in the design and fabrication innovations that lead to the high-sensitivity accelerometers and make a comparison of these in terms of their sensitivities and resolutions.

5.1. *Bulk micromachined piezo-resistive accelerometer (Roylance and Angell, 1979)*[21]

It appears that the first bulk-micromachined accelerometer was made by Roylance and Angell (1979). It was a z-axis accelerometer consisting of a cantilever support holding a huge proof-mass. Piezo-resistors were embedded at the support end of the cantilever beam where the maximum strain is

Figure 15: The feedback combs with dc bias.
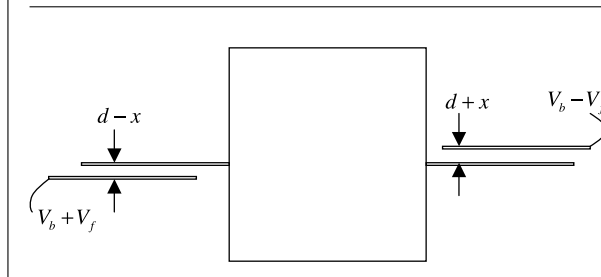
Figure 16: A bulk micromachined piezo-resistive accelerometer by Roylance and Angell[21] with schematic views from the side and the top.

experienced. Figure 16 shows a schematic of this accelerometer.

By using the linear beam theory for the suspension, the stiffness of this accelerometer can be obtained as

$$K_{st} = \frac{12EI_b}{l_b(4l_b^2 + 6l_m l_b + 3l_m^2)} \quad (30)$$

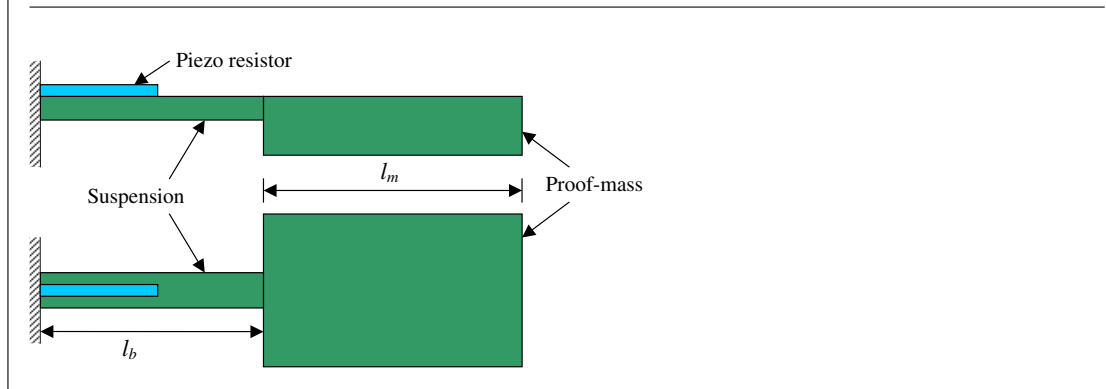where I_b is the area moment of inertia of the beam, E the elastic modulus, and l_m and l_b are as shown in Fig. 16.

Further improvement on the structure could have two or more beams on either side of the mass to reduce the cross-axis sensitivity. A similar structure could be used for capacitive sensing[41]. Two electrodes were patterned on glass slabs and wafer-bonded on the top and the bottom of the mass. Since small gaps are required for large sensitivities, the distance between the electrode and the mass should be small. Through slits on the wafer reduce damping that arises due to small gaps below the proof-mass. Wet etching in silicon (110) wafers helps obtain straight vertical side-walls on the wafer. A schematic is shown in Fig. 17.

Fabrication:

In Roylance an Angell' accelerometer, silicon wafers of (110) orientation were taken and wet-etched to determine the suspensions as well as the slits. The entire substrate thickness was used for the mass to increase its value. Finally, electrodes were deposited on the glass plates and they were wafer-bonded to the wet-etched silicon wafer so that differential capacitance could be sensed. The electrodes were used for both sensing as well as actuation in a closed-loop mode. The major processes required for this fabrication were wet etching and wafer bonding. Since these are simple processes, these types of accelerometers were popular and were batch-fabricated.

Advantages:
(a) Simple design and fabrication process.
(b) High base-capacitance of close to 20 *pF*, which helps eliminate the parasitic capacitance to a great extent.
(c) Low cross-axis sensitivity.
(d) Ability to incorporate slits that reduce damping.

Disadvantages:
(a) Low stiffness for inertial sensing is tough to obtain.
(b) Small gaps below the proof-mass are also not possible for inertial-grade sensitivity.
(c) Temperature-sensitivity is high if there is a mismatch in the coefficient of expansion of the glass plate and the silicon, which are bonded together.

5.2. *A capacitive accelerometer using pressure sensor fabrication technology - Rudolf et al. (1983)*[22]

This too is a *z*-axis accelerometer but uses a torsional suspension as shown in Fig. 18. As in the previous case, the electrodes were deposited on the glass plates and the glass plates were wafer bonded to the silicon chip. If *d*, *h* and *L* are the width, thickness and the length of the torsion bars, respectively, the torque required to twist the bar by unit radian is given by the formula:

$$\frac{T}{\alpha} = \frac{2Gdh^3}{3L} \quad (31)$$

The torque is related to the acceleration by the formula $T = a \int r\, dm$ where *r* is the distance of the differential mass *dm* from the rotational axis. The moving plate rotates about the torsional beams and thus creates a capacitance-change between the upper and lower electrodes.

Figure 17: Capacitive Z-axis accelerometer with quad-beam suspension.

Disadvantages:
(a) The entire device is of uniform thickness, thus the proof-mass is reduced.
(b) Vacuum packaging reduces the damping factor and thus even small vibrations do not die out quickly enough.

5.3. *Surface Micromachined Accelerometers.*
In the mid-1990's when the field of micro-electromechanical systems (MEMS) was attracting researchers' interest, there was a constant effort to integrate electronics as well as the inertial sensing components in the same chip. Thus, the complementary metal oxide semiconductor (CMOS) processes to fabricate surface micromachined accelerometers started to gain predominance because they were amenable for monolithic integration of electronics on the same chip. The monolithic integration had the advantage of good capacitance resolution and low parasitics. Furthermore, the power consumed by the entire device is low. Surface micromachining on the other hand, could give smaller gaps, and thus larger sensitivity, than the bulk micromachined accelerometers. However, these accelerometers could not be made to be of inertial-grade quality because of their poor sensitivity due to small size of the proof-mass. Furthermore, low stiffness and small gaps decrease the pull-in voltage, which reduce the sense voltage that can be applied for sensing. These accelerometers are best suited for batch-fabrication and for applications such as air-bag deployment in automobiles.

Surface-micromachined accelerometers can be for z-axis as well as $x - y$ axis acceleration signals. The z-axis accelerometers have high sense-capacitances, but suffer from squeeze-film damping[48]. The $x - y$ accelerometers suffer from low damping but require a number of comb drives to increase the base-capacitance. Fringing fields contribute to the majority of the capacitance in the $x - y$ axis accelerometers. Some of the popular $x - y$ as well as z-axis surface-micromachined accelerometers are discussed below.

Figure 18: Capacitive torsional silicon accelerometer[22].

Fringing fields: The crowding of the electric (or other) field lines at the corners and edges.

Fabrication:
This particular structure used the pressure sensor technology. A slightly p-doped silicon (100) wafer was back-etched up to a certain depth and then electrochemical etch-stop was used to thin the membrane further down. The etch-stop was obtained by doping (n-type) of the wafer before the process, which defines the suspension. Then, the electrodes were deposited on the glass plates and were wafer-bonded onto silicon and then diced. The entire device was vacuum-packaged.

Advantages:
(a) A very thin suspension is obtained which can reduce the stiffness of the device.
(b) Fabrication is easy and its repeatability is good due to the use of the electrochemical etch stop.
(c) Vacuum packaging reduces Brownian noise and thus increases the resolution of the device.

5.3.1. *A Z-axis surface-micromachined accelerometer with integrated CMOS circuitry - Lu et al. (1995)*[49]
The structure of this accelerometer consists of a rectangular mass with L-shaped beams in a pin-wheel arrangement as shown in Fig. 19. The L-shaped beams give very low stiffness in the z-direction and low cross-axis sensitivity. If l_b is the length of the beam and l_b its area moment of inertia, the stiffness of the entire structure with four beams is given by:

$$K_{str} = \frac{24EI_b}{l_b^3} \qquad (32)$$

Figure 19: Surface Micromachined z-axis accelerometer by Lu et al. (1995)[49].

Proof-mass

Suspension

Stiction: A contraction of "sticking friction" encountered in released micromachined structures that tend to stick to the substrate underneath.
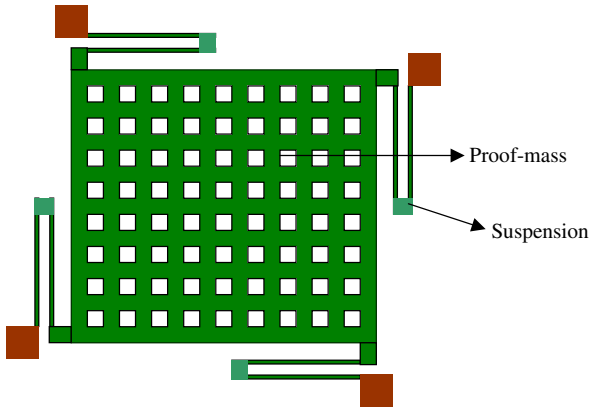
Fabrication:

This structure was fabricated by surface micromachining. First, an oxide layer of thickness equal to the desired gap between the electrodes was deposited. It is then patterned to define the anchors of the suspension. Then a polysilicon layer of the desired thickness was deposited and patterned to shape the mass and the suspension. Etch-holes, which help decrease damping, were then made. The sacrificial oxide is then etched away to release the proof-mass and the suspension.

Advantages:

(a) High sense-capacitance.
(b) Low stiffness leading to high sensitivity.

Disadvantages:

(a) Fabrication process needs to take care of the stiction problem.

Surface and bulk micromachining: Surface and bulk micromachining of silicon refer to two fundamentally different techniques in realizing shapes at the micron scale. In surface micromachining, thin films are deposited and etched on top of a silicon wafer or some other substrate to create layered microstructure. In contrast, in bulk micromachining, the silicon wafer (or another substrate) is carved (by chemical etching or by other means) to create desired geometrical features. The thickness of the micromachined structure is an order of magnitude larger in bulk micromachining than that in surface micromachining.

(b) Low stiffness leads to a low pull-in voltage.
(c) Low z-axis stiffness may also lead to sagging of the mass due to self-weight.
(d) Small gaps lead to large squeeze-film damping.

5.3.2. *Surface micromachined lateral (x − y) commercial accelerometer (ADXL-50) - (Kuehnel and Sherman, 1994)*[41]

This accelerometer, shown in Fig. 20, is one of the earliest of the accelerometers manufactured by Analog Devices Inc. It uses a surface micromachined proof-mass, suspension, and comb-drives for lateral sensing. The accelerometer was incorporated with a closed-loop circuit. The suspension used in this consisted of a pair of simple guided cantilevers on either side. If l_b is the length of each beam, and I_b is the area moment of inertia of the cross-section of the beam then the stiffness of the suspension is given by

$$K_{str} = \frac{48EI_b}{l_b^3} \quad (33)$$

The fabrication process of this accelerometer is similar to any typical surface micromachining process. Advantages of these types of accelerometers are that low stiffness is achievable without the problems associated with sagging due to self-weight.

5.4. ***Micro-g resolution accelerometers fabricated by a combination of surface and bulk micro machining- Chea et al. (2004-5)***[17,18]

It is evident from the previous examples that surface micromachining can provide low gaps and sufficiently flexible suspensions. However, low mass decreases the overall sensitivity and increases noise. Bulk-micromachining, on the other hand, provides a huge mass, a large capacitance area, but has the

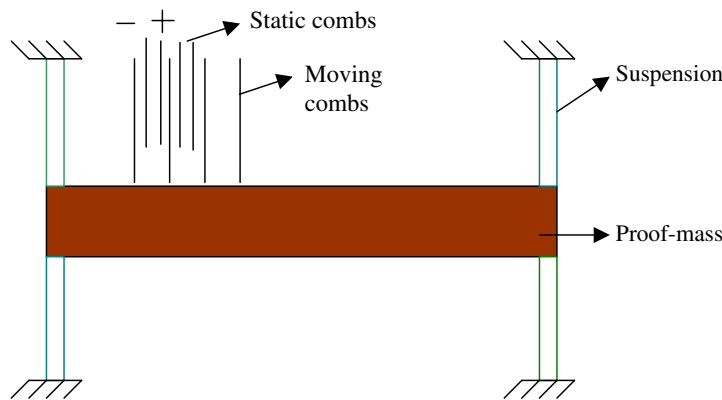Figure 20: ADXL 50 surface micromachined lateral accelerometer by Analog Devices, Inc.

Static combs

Moving combs

Suspension

Proof-mass

Figure 21: A high-sensitivity *z*-axis accelerometer using combined bulk and surface micromachining (re-drawn after reference [7]).
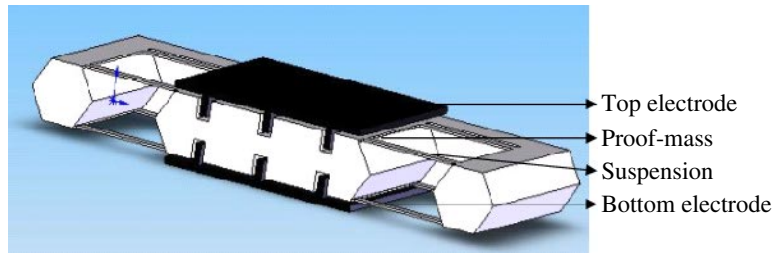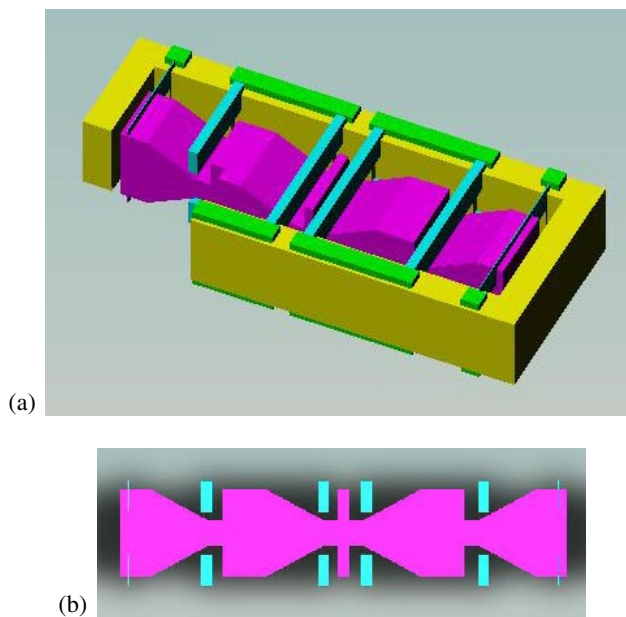

Figure 22: A high-sensitivity In-plane accelerometer using combined bulk and surface micromachining by Chae et al. (2004)[42] (a) A perspective view showing the proof-mass, suspension beams, comb-fingers that form the capacitors, and bond pads on the frame. (b) a cross-section view of the proof-mass, suspension beams, and the comb-fingers.

(a)

(b)

drawback of stiff suspensions and large minimum gaps. Then, the gradual evolution for accelerometers towards high resolution and sensitivity led to the combination of the advantages of surface and bulk micro machining processes where huge proof-mass could be obtained by bulk-micromachining while small gaps and suspension stiffness could be realized by surface-micromachining.

5.4.1. *A z-axis accelerometer using bulk and surface micromachining (Chae et al., 2004)*[7]

The proof-mass of this accelerometer, which is shown in Fig. 21, has an area of $2000 \times 2000 \mu m^2$. The thickness of the proof mass is 450 μm having a mass of 2.07 mg. There are eight suspension springs each 700 μm long, 3 μm thick, and 40 μm wide providing a stiffness of 14 N/m. The electrodes are at the top and bottom of the proof mass maintaining a gap of 1.5–2 μm. This gap was obtained by surface micromachining, i.e., by depositing poly-silicon on a sacrificial oxide layer. The electrode has considerable number of damping holes to reduce the mechanical noise. The electrode has vertical stiffeners to decrease its deflection under the internal forces.

5.4.2. *An In-plane accelerometer using bulk and surface micromachining (Chae et al., 2000)*[42]

The fabrication procedure for this accelerometer, which is shown in Fig. 22, is the same as that of

Table 2: A comparison of various capacitive accelerometers discussed in Section 5

Accelerometer structure (with reference)	A torsional capacitive accelerometer (Section 5.2)	Bulk micromachined capacitive accelerometer (Section 5.1)	Surface micromachined accelerometer (Section 5.3)	Accelerometer with combination of bulk and surface micromachining (Section 5.4)	Accelerometer with high aspect ratio etching using DRIE (Section 5.5)
Mass in kg	1e-9	4e-6	0.5e-9	2.76e-6	1.8216e-6
Stiffness N/m	0.158	572	0.94073	14	90.4
Natural frequency in Hz	2000	1835	7500	250	2140
Base Capacitance in pF	1	12.3	0.88	8	32.1
Sensitivity in $(\Delta C/C)/g$	0.04	0.0148	0.0052	0.25	0.0249
Resolution (assuming a circuit with 10 ppm resolution)	$250\mu g$	$650\mu g$	$1.9mg$	$1.5\mu g$	$400\mu g$

the above z-axis accelerometer shown in Fig. 21. Deep trenches were made on the proof mass and the electrodes were deposited in these trenches. The gap, obtained by sacrificial etching of the oxide, is around 2 μm. The stiffness of the suspension is given by

$$K_{stiff} = 96EI_b/l_b^3 \qquad (34)$$

where l_b is the length of the suspension length and I_b is the area moment of inertia of the suspension springs. The capacitance obtained in the lateral case is slightly less than that of the out-of-plane case. The sensitivities (i.e., the relative change in capacitance per applied g acceleration) of these accelerometers, expressed as the fractional change of the base capacitance, is reported to be 0.25, although calculations indicate that it can be as high as five.

5.5. A bulk-micromachined accelerometer using deep reactive etching technique (DRIE) Chae et al. (2005)[17]

The design of this accelerometer is very simple; it consists of a mass with comb drives on both sides of the mass as shown in Fig. 23. A gap of 2 μm ass obtained within the comb drives, the aspect ratio of 1:60 permits the thickness of the mass and the comb drives to be 120 μm. To overcome the disadvantage of large gaps obtained by traditional wet etching and wafer bonding techniques, a high aspect ratio etching technique called the DRIE (Deep- Reactive Ion Etching) was used by Chae et al. (2004)[7]. This process is a combination of alternate etching and deposition. The etching creates cavities into the wafer and deposition protects the sidewalls from being etched away. This process produces deep trenches with aspect ration of around 1:60. Thus, small but deep gaps between the fixed and the movable plates were realized in capacitive accelerometers.

Table 2 summarizes the physical and performance parameters of the high-resolution accelerometers described above. The physical dimensions determine the mass, stiffness and the base-capacitance. The natural frequency, sensitivity and the resolution are decided by the overall performance of the accelerometer. It can be noticed in Table 2 that less than 1 μg resolution is possible but its bandwidth is decreased to 250 Hz.

It was noted in Section 3 that the ability of the electronics circuitry to cancel amplifier offsets and noise determines the resolution of the electronic circuit. In the next section, we review the different types of capacitance measurement methods.

6. Capacitance Measurement Techniques

The displacement of the proof-mass due to an applied acceleration might be as small as a few Angstroms. The electronics circuitry has to be sensitive enough to detect such a small displacement. So, the capacitance-sensing circuit should be able to sense the capacitance-change in the range of femto to atto Farad. Various techniques are investigated for measuring such a minute change in capacitance. In this section, various capacitive sensing techniques are described first. This is followed by descriptions of both digital and analog closed-loop systems used in accelerometers.

6.1. Analog circuits

In micromachined accelerometers, a sensing circuit is designed to obtain low noise levels and high sensitivity. Operational Amplifiers are used in circuits to obtain high gain and thereby increase the sensitivity. But an op-amp itself contains many non-idealities such as input offset, $1/f$ noise, thermal noise, etc. Hence, challenge in designing sensing circuit for an accelerometer is in increasing the sensitivity while keeping the noise level low.

Figure 23: A DRIE in-plane accelerometer.
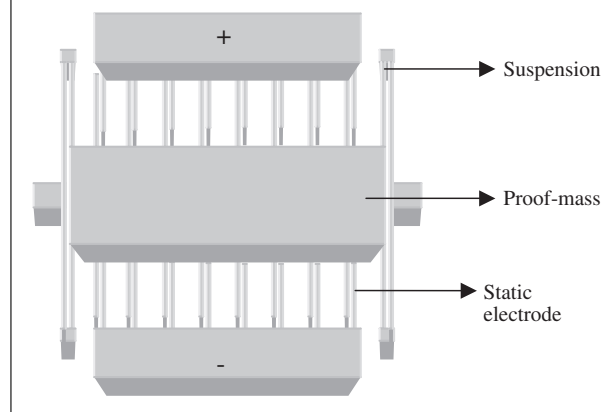
There are several capacitive sensing techniques that are used to detect changes in capacitance in an accelerometer. Some of them are:

1. Switched capacitor[19,47,49,50–56]
2. Correlated double sampling[45,52,57–59]
3. Chopper stabilization methods[50,60]

Switched capacitance is widely used to reduce the offset of the op-amp. In this technique the circuit offset is measured at a fixed time and is stored in a capacitor which can be later brought in series with the input in order to cancel the offset. Charging and discharging of the capacitor is controlled by the switches. This technique is also known as auto zeroing (AZ). This is a simple method to eliminate the offset.

At higher operating frequencies, the value of $1/f$ noise keeps on decreasing and it reduces below the thermal noise mark at some frequency. This frequency is known as the corner frequency. To remove all the noise, the auto zeroing frequency should be higher than the noise corner frequency. The residual noise is almost white. However, it is not equal to the thermal noise floor, as it is increased by the ratio of the unity-gain bandwidth of the amplifier and the auto zeroing frequency. The reason for this is that due to the sampling action, high-frequency components are folded back to the baseband. The higher the bandwidth of the amplifier, the more the sampled noise on the capacitor. The advantages and disadvantages of the switched capacitor technique are as follows:
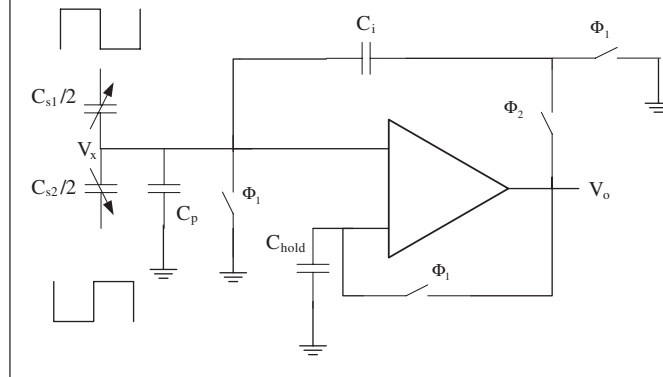
Advantages:
(a) Relatively easy to realize.
(b) Good for discrete, sampling based system.

Disadvantages:
(a) It suffers from noise folding.
(b) Overall noise level is more than the thermal noise floor.
(c) High kT/C noise at low capacitance.
(d) Suffers from switching noise.

Correlated double sampling (CDS) technique is an extension of the switched-capacitor technique. The CDS technique, which was originally introduced to reduce the noise produced in charged-coupled devices (CCD's)[58,59], can be described as an AZ operation followed by a S/H (sample and hold). It also reduces the $1/f$ noise along with the offset. The offset of an Op Amp is independent of the input signal, but $1/f$ noise depends on the input frequency. In this method, sampling is done twice in each cycle. First, the $1/f$ noise and the offset of the Op-Amp are stored in a capacitor. Next, the stored noise and offset are subtracted from a sample signal which is corrupted with $1/f$ noise and offset. One such circuit is shown below in Fig. 24. Here, the sense-capacitors (C_{s1} and C_{s2}) correspond to the differential capacitors of the accelerometer. During the first phase – the offset store phase – ϕ_1 is closed and ϕ_2 is open resulting in the storage of $1/f$ noise and offset onto the holding capacitor (C_{hold}). In the second phase – the signal amplification phase – the signal proportional to the difference between the two sense capacitors gets amplified and appears at V_o. Overall, CDS is superior in terms of noise reduction compared to simple switched capacitor circuit as it not only reduces the offset but also helps reduce the $1/f$ noise. But as it still relies on switched capacitors, it suffers from the switching noise. The advantages and disadvantages of the correlated double sampling technique are as follows.

Figure 24: Correlated double sampling technique.

Advantages:

(a) kT/C noise is reduced significantly.

(b) It can also be used to enhance the effective gain of the op-amp.

Disadvantages:

(a) It uses two phase switches which have to be controlled and timed precisely.

(b) It suffers from noise folding.

(c) Suffers from switching noise.

Chopper stabilization is based on modulation and demodulation principle. Initially, the signal modulates a high-frequency carrier (f_c), also called chopping, signal. The effect of $1/f$ noise and offset is eliminated by up-converting the signal to a high frequency. The sensed signal is then amplified at this high frequency. Finally, the signal is demodulated to the baseband signal. The chopping frequency is chosen such that Brownian noise instead of $1/f$ noise will decide the noise floor. This frequency is generally in the range of 1–2 MHz[60]. Consequently, the baseband noise of the chopper amplifiers is almost equal to Brownian white noise.

As the signal is modulated to a high frequency before passing trough Op Amp, it does not get affected by offset of the Op Amp because the offset is dc. When the signal is de-modulated, this dc offset gets modulated to a high frequency which can be filtered out. This way, the signal is always kept away from the offset to reduce the effect of the offset on the signal. The principle of chopper stabilization is depicted pictorially in Fig. 25. Here u is input signal, n the noise, $p(t)$ is the modulating signal and $p(t - t_0)$ is the de-modulating signal which is delayed version of $p(t)$, to account for the signal propagation delay through the Op-Amp. For ease of implementation the chopping signal is square wave rather than sine wave. This results in

up-conversion of signal and subsequently the noise at odd harmonics of the chopping signal. However all the higher harmonics are filtered out using a low-pass filter[60].

As shown in Fig. 25, modulating signal p can take values between $+1$ or -1, If n is noise signal at the low frequency, then $p^2 = 1$ and the output $y = (up + n)Ap = uA + A(np)$. Thus, the amplified signal is in the base-band but the amplified noise is up-converted to high frequency through multiplication by p. If p has period T_p with 50% duty cycle, its Fourier coefficient denoted by P_k is given by[60].

$$P_k = \frac{1}{T_p} \int_0^{T_p} P(t) e^{-jk(2\pi/T_p)t} dt$$

$$= \frac{2}{jk\pi} \qquad \text{if } k = \pm 1, \pm 3, \pm 5, \dots$$

$$= 0 \qquad \text{if } k = 0, \pm 2, \pm 4, \dots \quad (35)$$

If $S_n(\omega)$ denotes the power spectral density (PSD) of n, then PSD of pn becomes

$$S_{pn}(\omega) = \frac{4}{\pi^2} \sum_{k=-\infty}^{\infty} \frac{1}{(2k+1)^2} S_n\left(\omega - (2K+1)\frac{2\pi}{T_p}\right)$$

(36)

Thus, the effect of S_n is strongly reduced in baseband.

The circuit realization of chopper stabilization can be done in various ways. One of them is by arranging switches at the input of amplifier to alternately route the signal to $+$ and $-$ inputs of the Op-Amp . Thus the input is alternately multiplied by $+1$ and -1. The output of this circuit is demodulated. Demodulation is done either by using the same kind of switching arrangement or by using a multiplier circuit. Finally, the output is filtered to remove the offset component of the
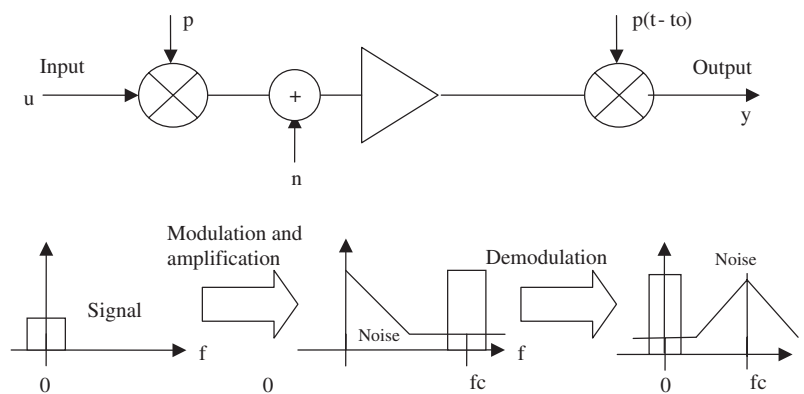
Figure 25: Chopper stabilization principle.

signal. High order low-pass filtering such as 3rd or 5th order Butterworth or any other active filter is generally used. The cut off frequency of the filter should be more than highest frequency expected at the input but less than chopping frequency. The advantages and disadvantages of the chopper stabilization technique are as follows.

Advantages:
(a) Noise floor is decided by white noise instead of $1/f$ noise.
(b) Good choice for continuous time system like MEMS based accelerometer where low baseband noise is an important requirement.
(c) Unlike the AZ technique, the chopper modulation does not introduce aliasing of the broadband noise.

Disadvantages:
(a) Effective gain of the op-amp is usually slightly reduced.
(b) Suffers from switching noise.

6.2. Analog feedback
Although analog feedback has been discussed earlier as an example of a closed-loop system, in this sub-section the electronics aspect of the analog feedback is discussed. In analog feedback, the feedback is proportional to the sensor output. The constant of proportionality is such that it counters the force applied and tries to bring the proof-mass to nominal position. This force acts as an equivalent electrical stiffness. All the forces—viz., damping, stiffness and electrical feedback—co-exist and act simultaneously on the proof mass. But in order to get negligible displacement even when constant force is applied, the feedback force has to be integrated before being applied to the proof-mass. This can be done by

introducing proportional-integral (PI) controller in the feedback. The block diagram of such an analog force feedback system is as shown in Fig. 26 [37].

Finding exact values of K_p and K_i is an iterative method. For tuning PID many methods are available to start with better approximated values. One of them is Ziegler–Nichols Step–Response Method. The step-response of the system can be predicted using a software tool such as Simulink[61]. Here, we get approximate values of K_p and K_i based on open-loop step-response of the system. Based on this approximate value, the PID gains can be fine-tuned to meet specific parameters such as the final displacement of the proof-mass or the response time.

The main advantage of using analog feedback loop is that it does not have the problem of limit cycles that we see in digital feedback loops. Furthermore, unlike digital loop, analog closed-loop accelerometers do not require additional signal processing after the final sense-signal is obtained. Additionally, the proof-mass is not subjected to high frequency oscillations as there are no limit cycles. The only disadvantage of analog closed-loop is that the final output signal is analog. Digital signal is always a preferred form of final output as digital signal is easy to transmit and store. Furthermore, an analog signal is more vulnerable to noise.

6.3. Digital feedback (Use of Sigma-delta modulation)
In 1962–63, Inose and Yasuda published two important papers[62,63] in which they introduced the concept of the single-bit-coding method. The basic idea was to have an integrator followed by a delta modulator with negative feedback. That was the first basic first-order sigma delta modulator. Though it was introduced as a coding method, it

Figure 26: Block diagram of analog force feedback accelerometers (based on a reference[37]).
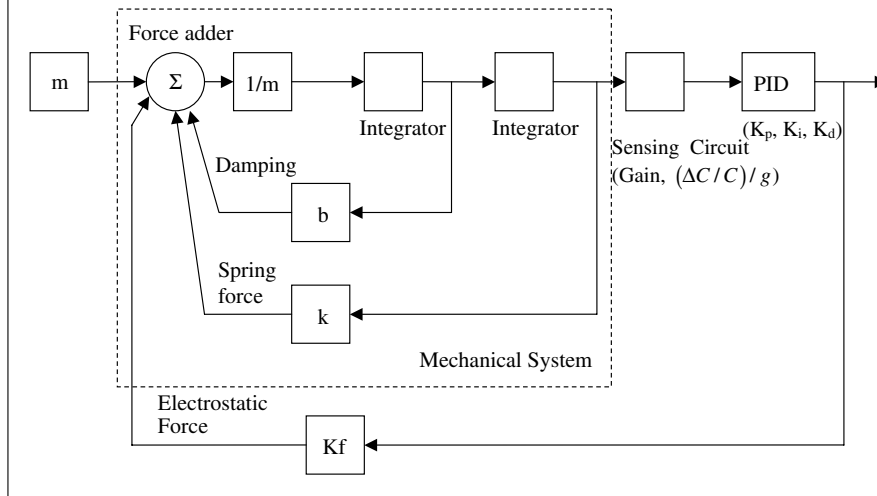
soon became popular as ADC/DAC at places where low or medium frequency and high resolution were required. Sigma-Delta ADC/DAC is an extension of the concept with the addition of a low pass filter after the modulator, which may be analog or digital depending on whether required output is digital or analog. As the VLSI technology progressed, the need for integrating more blocks on chip arose which made Sigma-Delta method popular. As its building blocks are simple, the Sigma-Delta modulation method became the first choice for designers in many low-frequency applications. With the advent of micromachined devices, the method found its application in accelerometers. The Sigma-Delta feedback was first applied to micromechanical element in a closed-loop accelerometer by Henrion in 1990[64]. The Sigma-Delta modulation system was selected because of its wide dynamic range possibilities. Use of a Digital Sigma-Delta modulator resulted in an all-digital closed-loop force-balance sensors.

The name Sigma-Delta modulator comes from putting the integrator (sigma) in front of the delta modulator[65]. As expected, there is an integrator ahead of a comparator, which acts as normal delta modulation, and there is a feedback through DAC. The final signal is passed through a filter for decimation. The filter can be either digital or analog depending on the type of the signal we need at the output.

Figure 27 shows a simple block diagram of a first order Sigma-Delta Analog-to-Digital Converter (ADC). The input signal X comes into the modulator via a summing junction. It then passes through the integrator, which feeds a comparator that acts as a one-bit quantizer. The comparator output is fed back to the input-summing junction via a one-bit digital-to-analog converter (DAC). The signal also passes through the digital filter and emerges at the output of the converter. The feedback loop forces the average of the signal W to be equal to the input signal X (see Fig. 24). The in-band noise power and the signal-to-noise ratio is given by[29]

$$\sigma_{ey}^2 = \sigma_e^2 \frac{\pi^2}{3} \left(\frac{2f_B}{f_s} \right)^3 \tag{37}$$

And SNR in dB is given as follows.

$$SNR = 10\log(\sigma_x^2) - 10\log(\sigma_e^2)$$
$$- 10\log\left(\frac{\pi^2}{3} \right) + 30\log\left(\frac{f_s}{2f_B} \right) (\text{dB}) \tag{38}$$

Assuming an over-sampling ratio, $\frac{f_s}{2f_B} = 2^r$, Eq. (37) becomes

$$SNR = 10\log(\sigma_x^2) - 10\log(\sigma_e^2)$$
$$- 10\log\left(\frac{\pi^2}{3} \right) + 9.03r (\text{dB}) \tag{39}$$

It can be seen from Eq. (39) that for every increment in r, SNR improves by 9 dB, equivalent to a resolution increment by 1.5 bits. Similarly it can be shown that if second order sigma-delta modulation is used, SNR increases by 15 DB, equivalent to resolution increment by 2.5 bits. This is the advantage of using sigma delta over all other digital modulation techniques.

The Sigma-Delta feedback was first applied to Micromechanical element in a closed loop

Figure 27: First order sigma delta ADC.
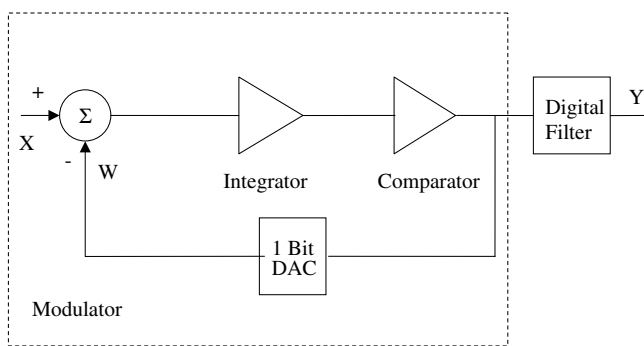
accelerometer by Henrion[64]. The basic block diagram an accelerometer that uses a Sigma-Delta modulator can be represented as shown in Fig. 28[37].

The Sigma-Delta modulation involves two important techniques namely over-sampling and noise-shaping. It is known that for a faithful reproduction of any signal, it needs to be sampled at a frequency higher than the Nyquist rate, which is twice the bandwidth of signal. The basic idea of over-sampling is to trade-off resolution in time for resolution in voltage. This means that when the signal is sampled at a rate much higher than the Nyquist rate, the samples are averaged to give better resolution at the output. The output of the Sigma-Delta modulator, therefore, has to be down-sampled to the base-band frequency. That is done through a special type of filter called the decimation filter. Decimation filter can be on-chip or it can be off-chip using a signal processing algorithm. Various

approaches of decimation filter design are available in the literature[66,67].

The main advantage of the Sigma-Delta feedback is that it gives digital output. In certain cases, if limit cycles are controlled properly, it also gives better resolution than analog closed-loop accelerometer. But as mentioned earlier, it requires extra-decimation filter and it suffers from limit cycles which is a kind of instability. There are a few ways to reduce the limit cycles to have improved minimum detectable displacement due to the applied acceleration. In the next sub-section we will see how to reduce the limit cycles.

6.3.1. *Limit Cycles*

The presence of nonlinear elements in the feedback loop can produce stable bounded oscillation called a limit cycle, Here, the nonlinearity of one-bit quantiser gives rise to a limit cycle. Force feedback is unstable without compensation because of the 180° phase delay from sensing element for frequencies above the resonant frequencies. There are three approaches to solve this issue, namely, electronically limiting the loop-bandwidth; over-damping the proof-mass[69]; and compensating with a lead filter[49,64].

The first approach uses electronic low-pass filter to reduce the loop-bandwidth to a frequency well below the resonance frequency of the proof-mass. But this technique is applicable only in situations where low sensitivity and limited bandwidth are tolerable. Thus, it reduces some benefits of feedback. The second solution is simple but, because of high Brownian noise floor of an over-damped low mass-sensing element, it is practical only for low-performance applications. The third approach of

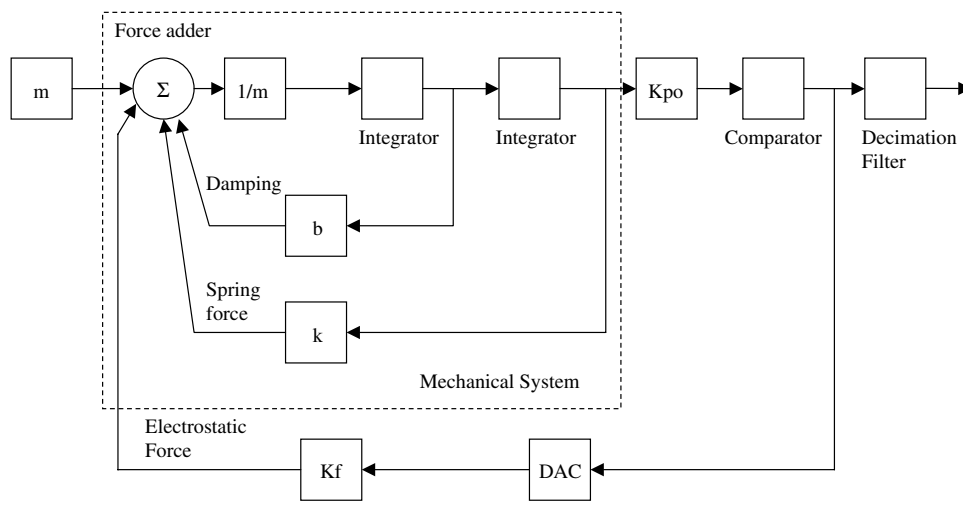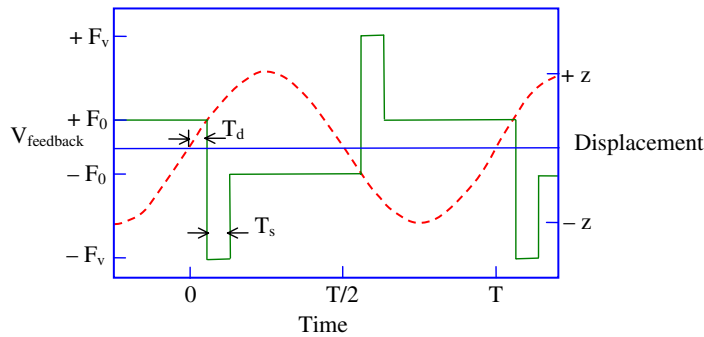Figure 28: Block diagram of force feedback digital accelerometers.

Figure 29: Limit Cycle waveforms of linearised feedback force with compensation (solid lines) and vertical displacement (Dashed line)[70].

using a compensation filter requires extra circuitry but there are no other trade-offs involved in it. The basic strategy is to add a left-half plane zero to the loop transfer function in order to decrease the phase delay at unity gain frequency. A limit cycle waveform with lead compensation is shown in Fig. 29.

Kraft[37] has predicted some tendencies in the comparison of limit cycles, which imply that, for frequencies much smaller than that of the limit cycle, flat frequency response and linear transfer characteristic are expected; and higher the sampling frequency higher the limit cycle frequency hence the higher the bandwidth of the transducer. Furthermore, for higher limit cycle modes a lower cut-off frequency is expected, and finally, an increase in the feedback voltage results in an increase in the bandwidth.

A limit cycle can be found by mathematical analysis by deriving the transfer function of the feedback loop[39]. There is another digital signal processing approach for finding limit cycles used by Colinet et al.[68] where they used two-step methods. The first step is the determination of system's response for a candidate limit cycle, which is done by Tsypkin or Hamel's Method. Software implementations of these methods were done through FFT algorithms. In the second stage, the consistency of sign-change at comparator input with those of candidate limit cycle is verified.

6.3.2. Recent Developments

The CMOS technology scaling in the last few years has continuously improved the speed of the transistor and the circuits built thereof. The 65 nm CMOS technology has enabled the tera Hz transistors. Since the Sigma-Delta technique exploits the resolution in time to provide a very high resolution in voltage, the performance of Sigma-Delta converters has steadily improved over the last

several years with very high frequency and high resolution converters implemented in a variety of applications[71,72]. Recently a higher order Sigma-Delta micro-g accelerometer has been realized with a capacitive resolution of 2 aF and with a dynamic range of 95 dB at 20 Hz[73]. It appears that the digital feedback with Sigma-Delta modulator will become a preferred technique to implement the closed loop accelerometers, with further improvements in the CMOS technology in future.

7. Summary, Recent Developments, and Future Trends

In this paper, an attempt has been made to enunciate various aspects of micromachined accelerometers that help in achieving a very fine resolution. Some of the salient points noted regarding achieving high resolution are summarized below.

(a) The resolution of the accelerometer is mainly limited by the electronic and the mechanical noise floors.

(b) These noise floors have a strong dependence on the frequency of operation (bandwidth) of the system.

(c) Electronic noise dominates the mechanical noise in most analog and digital accelerometers, and thus requiring a high mechanical sensitivity to overcome the electronic offsets and noise.

(d) A high mechanical sensitivity requires bulky proof-mass and flexible suspensions, thus reducing the bandwidth of the system.

(e) Microfabrication processes which make use of a combination of surface and bulk micromachining processes help in achieving a high mechanical sensitivity.

(f) Improved bandwidth, linearity, and range can be obtained by operating the accelerometer in a force re-balance mode. Feedback can be either analog or digital.

Figure 30: An Accelerometer with a displacement-amplifying compliant mechanism (DaCM)

External suspension

Sense-combs

Displacement-amplifying compliant mechanism (DaCM)

Proof-mass

Suspension
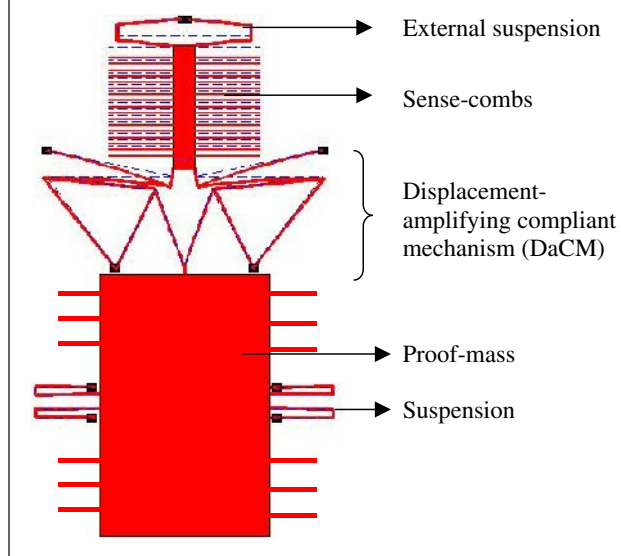
Dithering: Dithering is a process of adding a small amount of random noise, with amplitude that is half of the least significant bit, to minimize the effect of quantization noise. However, the white noise floor increases slightly, which may be tolerable in a variety of applications.

(g) Electronic noise is overcome by a number of techniques such as chopper stabilization, co-related double sampling, etc. Capacitance change as low as 2 *aF* can be detected. Electronic noise can be reduced to 100 nV.

Overall, miniaturization of micro-*g* resolution accelerometers is possible within the capabilities of the microfabrication technology. Better noise cancellation techniques and methods to increase the mechanical sensitivity are worth investigating to achieve micro-*g* and sub micro-*g* resolutions over a wide bandwidth.

Since an accelerometer involves many specialized fields such as structural mechanics, structural optimization, microfabrication, capacitive sensing, signal processing, and feedback control systems, new developments in any of them will contribute to improvement in its performance. Mechanical sensitivity can be enhanced with a large proof-mass and a flexible suspension. Recent developments have shown that a combination of surface and bulk micromachining processes are able to give the required proof-mass thickness and suspension stiffness, thus achieving micro-*g* resolution within a chip area of 2 mm × 1 mm. Though the sensitivity of such structures is high, their natural frequency is low, thus decreasing their bandwidth. To overcome this problem, a displacement-amplifying compliant mechanism (DaCM) can be used to amplify the displacement of the proof-mass to increase its sensitivity[74,75]. The displacement is sensed from the output portion of the DaCM, where the sense-combs are placed. The inertia at the output of the

DaCM, which displaces by a large amount, is very small compared to the proof-mass. Thus, its natural frequency is larger than that of the conventional accelerometers with the same sensitivity. However, the flexibility of the output of the DaCM leads to large cross-axis sensitivity, which can be limited by adding a suspension at this location. Figure 30 shows such an accelerometer with a DaCM. When, using such a device in the force re-balance mode, feedback has to be applied to the proof-mass and the sense-combs at the output of the DaCM[75].

On the electronics front, there have been attempts to reduce offset up to 100 nV using nested chopper stabilization[76]. Such a development in terms of offset and noise reduction can be applied to the accelerometer. Similarly, there have been attempts to increase sensitivity by introducing dithering to increase resolution[77]. Recently, there has been work on using floating gate transistors in sensing circuits, with a claim to improve performance in terms of improving SNR and reducing power consumption[78,79]. There has also been a development of simple one-mask process using thin-film SOI technology[80]. Thus, despite several decades of research in this area, it is still a dynamic field to work on and to apply various new ideas. Further research and increased use of the high-resolution accelerometers might help in bringing their cost down.

References
1. S. Y. Yurish, N. V. Kirianaki, I. L. Myshkin, " World sensors and MEMS Market : Analysis and trends", Sensors and Transducers Magazine (S&T e-digest), Vol. 62, Issue 12, Dec. 2005, pp. 456–461.
2. J. Waldorff, W. Gessener (Ed.), "Advanced Microsystems for Automotive Applications 2005", Springer Berlin Heidelberg
3. R. H. Grace, "Application Opportunities of MEMS/MST in the Automotive Market: *The Great Migration from Electromechanical and Discrete Solutions*", available online at www.rgrace.com.
4. G. A. Macdonald, "A review of low-cost accelerometers for vehicle dynamics", Sensors and Actuators A, 1990, Vol. 21, no. 1–3, pp. 303–307.
5. O. B. Degani, D. J. Seter, E. Socher, Y. Nenirovsky, "Comparitive study of novel micromachined accelerometers employing MIDOS", Sensors and Actuators, Vol. 80, 2000, pp. 91–99.
6. F. Rudolf, A. Jornod, J. Bergqvist and H. Leuthold "Precision Accelerometers with mu-g resolution," Sensors and Actuators, Volume 21A, Issues 1–3 , February 1990, pp. 297–302.
7. J. Chae, H. Kulah, and K. Najafi, An In-Plane High-Sensitivity, Low-Noise Micro-g Silicon Accelerometer With CMOS Readout Circuitry, Journal of Microelectromechanical Systems, Vol. 13, No. 4, August 2004
8. B.V. Amini, R. Abdolvand, and F. Ayazi, "A 4.5-mW Closed-Loop Δ Σ Micro-gravity CMOS SOI Accelerometer, IEEE Journal of Solid-State Circuits, Vol. 41, No. 12, 2006, pp. 2983–2991.
9. B.V. Amini and F. Ayazi, "Micro-gravity capacitive silicon-on-insulator accelerometers," *J. Micromech. Microeng.*, vol. 15, no. 11, pp. 2113–2120, Nov. 2005.

10. P. Monajemi and F. Ayazi, "Design optimization and implementation of a microgravity capacitive HARPSS accelerometer," *IEEE Sensors J.*, vol. 6, no. 1, 2006, pp. 39–46.

11. E. B. Cooper, E. R. Post, S. Griffith, J. Levitan, S. R. Manalis, M. A. Schmidt, and C. F. Quate, "High-resolution Micromachined Interferometric Accelerometer," Applied Physics Letters, Vol. 76, No. 22, 2000, pp. 3316–3318.

12. N. C. Loh, M. A. Schmidt, and S. R. Manalis, "Sub-10 cm^3 Interferometric Accelerometer with Nano-g Resolution," Journal of Microelectromechanical Systems, Vol. 11, No. 3, 2002, pp. 182–187.

13. H. Kulah, J. Chae, and K. Najafi, "Noise analysis and characterization of a sigma-delta capacitive silicon micro accelerometer", IEEE journal of solid-state circuits, Vol. 41, No.2, Feb 2006.

14. N. Yazdi and K. Najafi, "An all-silicon single-wafer micro-g accelerometer with a combined surface and bulk micromachining process", Journal of Microelectromechanical systems, Vo. 9, No. 4, December 2000, pp. 544–550.

15. C.-H. Liu, A. M. Barzilai, J. K. Reynolds, A. Partridge, T. W. Kenny, J. D. Grade, and H. K. Rockstad, "Characterization of a High-Sensitivity Micromachined Tunneling Accelerometer with Micro-g Resolution", *Journal of Microelectromechanical Systems*, Vol. 7, No. 2 (1998) pp. 235–44.

16. C.-H. Liu and T. W. Kenny, "A High-Precision, Wide-Bandwidth Micromachined Tunneling Accelerometer", *Journal of Microelectromechanical Systems*, Vol. 10, No. 3 (2001) pp. 425–33.

17. J. Chae, H. Kulah, and K. Najafi, "A monolithic three-axis micro-g micromachined silicon capacitive acceleroemter", Journal of Microelectromechanical systems, vol. 14, No. 2, April 2005, pp. 235–242.

18. J. Chae, H. Kulah, and K. Najafi, "An In-Plane High-Sensitivity, Low-Noise Micro-g Silicon Accelerometer with CMOS Readout Circuitry," *IEEE/ASME Journal of Microelectromechanical Systems (JMEMS)*, vol. 13, no. 4, p 628–635, August, 2004.

19. X. Jiang, F. Wang, M. Kraft, and B.E. Boser, " An Integrated Surface Micromachined Capacitive Lateral Accelerometer with $2\mu g/\sqrt{Hz}$ resolution", proceedings of the Solid-state, Actuator and Microsystems Workshop, Hilton Head Island, South Carolina, June 2–6, 2002, pp. 202–205.

20. J. Willis and B.D. Jimerson, "A Piezoelectric Accelerometer," Proceedings of the IEEE, Correspondence, 1964, pp. 871–872.

21. L. M. Roylance and J. B. Angell, A batch-fabricated silicon accelerometer, IEEE Tran. Electron Dev., ED-26 (1979) 1911.

22. F. Rudolf , A Micromechanical Capacitive Accelerometer With a Two-Point Inertial Mass suspension, Sensors and Actuators, 4(1983) 191–198

23. D. L. DeVoe, A. Pisano, "A fully surface micromachined piezoelectric acceleroemter", proceedings of the International Conference on solid-state sensors and actuators, Chicago, June-15-16,1997, pp. 1205–1208.

24. E. Abbaspour-Sani, R. S. Huang, and C. Y. Kwok, "A linear electromagnetic accelerometer," *Sensors Actuators A*, vol. 44, pp. 103–109, 1994.

25. T. W. Kenny, S. B. Waltman, J. K. Reynolds, and W. J. Kaiser, "Micromachined silicon tunnel sensor for motion detection", Applied physics letters, Vol. 58 (1), 1991.

26. C. Yeh and K. Najafi, "CMOS interface circuitry for a low-voltage micromachined tunneling accelerometer", Journal of microelectromechanical systems, Vol. 7, No. 1, March 1998, pp. 6–14.

27. C. Yeh and K. Najafi, "A low-voltage tunneling based silicon microaccelerometer", IEEE transactions of electron devices, Vol. 44 , No. 11, 1997, pp. 1875–1882.

28. H. K. Rockstad, T. K. Tang, J. K. Reynolds, T. W. Kenny, W. J. Kaiser and T. B. Gabrielson, "A Miniature, High-Sensitivity, Electron Tunneling Accelerometer", *Sensors and Actuators A*

53, (1996) pp. 227–31.

29. R. L. Kubena, G. M. Atkinson, W. P. Robinson, and F. P. Stratton, "A New Miniaturized Surface Micromachined Tunneling Accelerometer", *IEEE Electron Device Letters*, Vol. 17, No. 6 (1996), pp. 306–308.

30. E. Abbaspour-Sani, R.S. Hwang, C.S. Kwok., "A Novel Optical Accelerometer", IEEE Electron Device Letters, vol. 16, No. 5, May 1995, pp. 166–168.

31. C. Pedersen and A. Seshia, 2004, "On the optimization of compliant force amplifier mechanisms for surface micromachined resonant accelerometers", *IOP Journal of Micromechanics and Microengineering*, Vol. 14, No. 10, pp. 1281–1293.

32. X. P. S. Su and H. S. Yang, 2001, "Two-stage compliant micro-leverage mechanism optimization in a resonant accelerometer", *Structural and Multidisciplinary Optimization,* Vol. 22, pp. 328–336.

33. F. Mailly, A. Giani, A. Martinez, R. Bonnot, P. Temple-Boyer, and A. Boyer, "Micromachined thermal accelerometer", Sensors and Actuators A, 103 (3) (2003), pp. 359–363.

34. M. H. Bao, 2000, *Handbook of Sensors and actuators – Accelerometers and Pressure sensors* , Elsevier publication

35. N. Yazdi, F. Ayazi, and K. Najafi, "Micromachined Inertial Accelerometers", Proc. IEEE, vol. 86, pp. 1640–1658, 1998

36. R. P. van Kampen, M. J. Vellekoop and P. M. Sarro, R. F. Wolffenbuttel, "Application of electrostatic feedback to critical damping of an integrated silicon capacitive accelerometer", Sensors and Actuators A, Vol. 43, 1994, pp. 100–106.

37. M. Kraft, 1997, "Closed loop digital accelerometer employing over-sampling conversion", PhD Dissertation, Coventry University.

38. W. Yun and R. T. Howe, "Silicon micromachined accelerometers: a perspective on recent developments", Sensors Expo Poceedings, Chicago, Il, USA, 1991, pp. 204A/1-204A/8.

39. W. T. Thomson and M.D. Dahleh, 1997, *Theory of Vibration with Application*, Prentice Hall, 5th Edition.

40. S. D. Senturia, 2000, *Microsystems Design*, Kluwer Academic Publishers.

41. W. Kuehnel and S. Sherman, "A surface micromachined silicon accelerometer with on-chip detection circuitry", Sensors and Actuators A, Vol. 45, 1994, pp. 7–16.

42. J. Chae, H. Kulah, and K. Najafi, "A hybrid silicon-on-glass (SOG) lateral micro-accelerometer with CMOS readout circuitry", Journal of microelectromechanical systems, vol. 9, 2000, pp. 544 -550.

43. M. Stephens, "A Sensitive Interferometric Accelerometer," *Rev. Sci. Instrum.*, vol. 64, no. 99, pp. 2612–2614, 1993.

44. Analog Devices, Inc., "Low-Cost ±2g Dual-Axis Accelerometer with Duty Cycle Output-ADXL202E", available online at www.analogdevices.com.

45. B.E Boser and R.T. Howe "Surface Micromachined Accelerometer" IEEE Journal of Solid state Circuits , Vol. 31 No. 3 pp 366–75.

46. T. B. Gabrielson, 1993, "Mechanical-thermal noise in micromachined acoustic and vibration sensors", *IEEE Transactions on Electron Devices*, vol. 40, pp. 903–909.

47. H. Kulah, Navid, and K. Najafi " A CMOS Switched-Capacitor Interface Circuit for an Integrated Accelerometer" Proc. 43rd IEEE Midwest Symp. on Circuits and Systems, Lansing MI, Aug 8–11,2000.

48. R. Pratap, S. Mohite, and A.K. Pandey, "Squeeze film effects in MEMS Devices," Journal of the Indian Institute of Science, Vol. 87, No. 1, 2007, pp. 75–94.

49. C. Lu, M. Lemkin, B. E. Boser, "A monollithic surface micromachined acceleroemter with digital output", Journal of solid-state circuits, Vol. 30, No. 12, Dec. 1995, pp. 1367–1373.

50. C. C. Enz and G. C. Temes, "Circuit techniques for reducing the effects of Op-Amp imperfections: Autozeroing, correlated,

double sampling and chopper stabilization," Proceedings of the IEEE , vol. 84, no. 11, pp. 1584–1614, November 1996.

51. S. Kim, Y. Yee, H. Kim, and K. Chun, "A CMOS-compatible Silicon Accelerometer with Polysilicon Rib-style Flexures," Microprocesses and nanotechnology Conference, Issue 13-16, July 1998, pp. 176-177.

52. M. Lemkin and B. E. Boser, "A three-axis micromachined accelerometer with a CMOS position-sense interface and digital offset-trim electronics," *IEEE J. Solid State Circuits*, vol. 34, pp. 456–468, Apr. 1999.

53. T. Smith, O. Nys, M. Chevroulet, Y. DeCoulon, and M. Degrauwe, " A 15 b electromechanical sigma-delta converter for acceleration measurements," 41st IEEE International Solid-State Circuits Conference, 1994. Digest of Technical Papers. 16–18 Feb. 1994, pp 160–161.

54. N. Yazdi and K. Najafi, "An interface IC for a capacitive μg accelerometer," IEEE International Solid-State Circuits Conference, 1999. Digest of Technical Papers. ISSCC. 1999, pp 132–133.

55. J. Chae, H. Kulah, and K. Najafi, "An in-plane high-sensitivity, lownoise micro-G silicon accelerometer," *Proc. 16th IEEE Int. Conf. Micro Electro Mechanical Systems (MEMS 2003)*, Kyoto, Japan, 2003, pp. 466–469.

56. H. Kulah, J. Chae, N. Yazdi, and K. Najafi, "A multi-step electromechanical converter for micro-g capacitive accelerometers," in *IEEE Int. Solid-State Circuits Conf. Dig. Tech. Papers*, San Francisco, CA, 2003, pp. 202–203.

57. N. Wongkomet and B.E. Boser "Correlated Double Sampling in Capacitive Position Sensing Circuits for Micromachined Applications", IEEE Asia-Pacific Conference on Circuits and Systems, 1998. IEEE APCCAS 1998., Publication Date: 24–27 Nov 1998 pp 723–726.

58. K. H. White, D. R. Lampe, F. C. Blaha, and I. A. Mack, "Characterization of surface channel CCD image arrays at low light levels." *IEEE J. Solid-State Circ.,*, vol. 9, pp. 1–14. Feb. 1974

59. R.W. Brodersen and S. P. Emmons, "Noise in buried channel charge-coupled devices," *IEEE J. Solid-State Circ.,* vol. 11, pp. 147–156, Feb. 1976.

60. L. Tóth and Y. P. Tsividis, "Generalization of the Principle of Chopper Stabilization" , IEEE Transactions on Circuits and Systems I: Fundamental Theory and Applications Aug. 2003 Volume: 50, Issue: 8 pp 975–983.

61. Simulink: Control Systems Simulation Module in Matlab, www.mathworks.com

62. H. Inose and Y. Yasuda, "A unity bit coding method by negative feedback" Proceedings of the IEEE Volume 51, Issue 11, Nov. 1963 Page(s): 1524–1535

63. H. Inose, Y. Yasuda, Y, Y. Kawai, and M. Takagi, "The Subscriber-Line Circuit and the Signaling and Tone System for an Experimental Time-Division Exchange Featuring Delta-Modulation Techniques" Communications, IEEE Transactions on [legacy, pre - 1988]

64. W. Henrion, "Wide dynamic range direct digital accelerometer" Solid-State Sensor and Actuator Workshop, 1990. 4th Technical Digest., IEEE , 4–7 June 1990 pp 153–57.

65. S. Park "Principles of Sigma-Delta Modulation for Analog-to-Digital Converters" Motorola Digital Signal Processors APR8

66. J. Candy, "Decimation for Sigma Delta Modulation", IEEE Transactions on Communications Volume 34, Issue 1, Jan 1986 pp 72–76.

67. M. Sokolovic, B. Jovanovic, and M. Damnjanovic, "Decimation filter design" International Conference on Microelectronics Volume 2, Issue , 16–19 May 2004 pp 601–604.

68. E. Colinet, J. Juillard, S. Guessab, R. Kielbasa "Resolution Enhancement of a Sigma-Delta Micro-Accelerometer using Signal Prediction" International Conference on MEMS,

NANO and Smart Systems (ICMENS'04) 2004.

69. T. Kajita, U. Moon, and G. C. Temes "A noise- shaping accelerometer interface circuit for two-chip implementation " ISCAS 2000 - IEEE International Symposium on Circuits and Systems, May 28–31, 2000, Geneva, Switzerland pp IV 337–IV 340.

70. G.K Fedder "Simulation of Micromechanical systems" PhD Dissertation University of California Berkley 1994.

71. J, Arias, P. Kiss, V. Prodanov, V. Boccuzzi, M. Banu, D. Bisbal, J.S. Pablo, L. Quintanilla, and A. Barbolla, "A 32-mW 320-MHz continuous-time complex delta-sigma ADC for multi-mode wireless-LAN receivers" , IEEE Journal of Solid-State Circuits, Volume 41, Issue 2, Feb. 2006 pp. 339–351.

72. http://www.elecdesign.com/Articles/Index.cfm?AD= 1{\&}ArticleID=14105, "Analog Progresses On And Off The Beaten Path", Electronic Design.

73. B.V. Amini, R. Abdolvand, and F. Ayazi, "A 4.5mW Closed-Loop $\Delta\Sigma$ Micro-gravity CMOS-SOI Accelerometer" International Solid State Circuits Conference 2006.

74. G. Krishnan and G.K. Ananthasuresh. "An Objective Evaluation of Displacement-Amplifying Compliant Mechanisms for sensor applications" proceedings of the ASME-IDETC-CIE, Philadelphia PA, September 2006.

75. G. Krishnan, "Displacement-amplifying Compliant mechanisms for sensor applicaitons", Masters Thesis, Mechanical Engineering, Indian Institute of Science, Bangalore, India, 2007.

76. A. Bakker, K. Thiele, and J. H. Huijsing, "A CMOS Nested-Chopper Instrumentation Amplifier with 100-nV Offset", IEEE Journal of solid state circuits, VOL. 35, NO. 12, Dec. 2000 pp 1877–1883.

77. T. Kajita, U.-K. Moon, and G. C. Temes, "A Two-Chip Interface for a MEMS Accelerometer" IEEE transaction on instrumentation and measurement, VOL. 51, NO. 4, pp 853- 58, , Aug 2002.

78. S. Y. Peng M. S. Qureshi, A. Basu, P. E. Hasler, and F. L. Degertekin, "A Floating-gate Based Low-Power Capacitive Sensing Interface Circuit" IEEE Custom Integrated Circuits Conference 2006, 10–13 Sept. 2006 pp 257–260.

79. S. Y. Peng M. S. Qureshi, A. Basu, P. E. Hasler, and F. L. Degertekin, "High SNR capacitive sensing transducer" Circuits and Systems, 2006. ISCAS 2006. Proceedings. 2006 IEEE International Symposium on 21–24 May 2006 Page(s):4 pp. 1175–1178.

80. F. Iker, N. Andre, T. Pardoen, and J.-P. Raskin, "Three-Dimensional Self-Assembled Sensors in Thin-Film SOI Technology" Journal of Microelectromechanical Systems, Volume 15, Issue 6, Dec. 2006 Page(s): 1687–1697.

Girish Krishnan completed his Bachelors in Mechanical Engineering from R. V. College of Engineering, Bangalore in the year 2004 and masters (MSc) in Mechanical Engineering from Indian Institute of Science (IISc), Bangalore in 2006. He is currently pursuing his PhD in the Mechanical engineering department, University of Michigan, Ann Arbor. His areas of interests are Microsystems design, Compliant mechanisms and Topology optimization. He is a student member of the ASME (American Society of Mechanical Engineers).

Chaitanya Kshirsagar is BE in electronics and tele-communication from Government Engineering College, Aurangabad. He has worked as research scholar in microelectronics lab, electrical communication engineering department, Indian Institute of Science. His research interest includes capacitive sensing for MEMS devices, VLSI circuits and nanoscale devices. He is currently pursuing the Ph.D. degree in

electrical and computer engineering at the University of California, Santa Barbara.

G. K. Ananthasuresh obtained his B.Tech. degree in 1989 from IIT-Madras, M.S from University of Toledo, OH, USA, and Ph.D. in 1994 from the University of Michigan, Ann Arbor, MI, USA. He was a post-doctoral research associate in the Microsystems Technology Laboratories at M. I. T., Cambridge, MA, USA, before he joined the University of Pennsylvania's Mechanical Engineering and Applied Mechanics department in 1996 as an Assistant Professor and then promoted with tenure to Associate Professor in 2002. He joined the Indian Institute of Science (IISc) in 2004. His research interests include compliant mechanisms, microsystems multi-disciplinary design optimization, topology optimization, microfabrication, mechanism design and kinematics, protein modeling and design, micromanipulation, and bio-design. He has more than 125 publications out of which 46 are journal papers. He is also the author of six book-chapters and an edited book entitled "Optimal Synthesis Methods for MEMS". He has three best paper awards at international conferences and three patents. He is the recipient of the Swarnajayanthi Fellowship from the Department of Science and Technology, India; National Science Foundations' Early Career (CAREER) award by the National Science Foundation, USA; and the Society of Automotive Engineers' Ralph Teetor Distinguished Educator award. He served/serves on the editorial boards of four journals and is the editor of the Institute of Smart Structures and Systems (ISSS) newsletter, Sūkshma.

Navakanta Bhat received his B.E. in Electronics and Communication from University of Mysore in 1989, M.Tech. in Microelectronics from I.I.T. Bombay in 1992 and Ph.D. in Electrical Engineering from Stanford University, Stanford, CA in 1996. Then he worked at Motorola's Networking and Computing Systems Group in Austin, TX until 1999. At Motorola he worked on logic technology development and he was responsible for developing high performance transistor design and dual gate oxide technology. He joined the Indian Institute of Science, Bangalore in 1999 where he is currently an Associate Professor in the Electrical Communication Engineering department. His current research is focused Nano-CMOS technology and Integrated CMOS-MEMS sensors. The work spans the domains of process technology, device design, circuit design and modeling. He has several research publications in international journals and conferences and 3 US patents to his credit. He has received the Young Engineer Award (2003) from the Indian National Academy of Engineering. He is also the recipient of the Swarnajayanti fellowship (2005) from the Department of Science and Technolgy, Govt. of India and Prof. Satish Dhavan award (2005) from the Govt. of Karnataka. He was the founding chair of the IEEE Electron Devices and Solid-State Circuits society, Bangalore chapter which was recognized as the Outstanding Chapter of the Year by the IEEE SSC society (2003) and IEEE EDS society (2005). He has been on the program committees of several international conferences. He was the technical program chair for the international conference on VLSI design and Embedded systems (2007). He is a Distinguished Lecturer of the IEEE Electron Devices Society.